The Thesis Committee for Christopher Yoon
Certifies that this is the approved version of the following Thesis:

Evaluation of Film Cooling Superposition Method on the Suction Side of a Blade Model

APPROVED BY
SUPERVISING COMMITTEE:

David Bogard, Supervisor

Ofodike Ezekoye

Evaluation of Film Cooling Superposition Method on the Suction side of a Blade Model

by

Christopher Yoon

Thesis

Presented to the Faculty of the Graduate School of

The University of Texas at Austin

in Partial Fulfillment

of the Requirements

for the Degree of

Master of Science in Engineering

The University of Texas at Austin

December 2018

Dedication

To my parents, my neighbors, and my espresso machine. Thank you for your support.

Acknowledgements

I would like to thank Dr. Bogard for his guidance throughout my journey. His vast wisdom and guidance led many graduate students, but I believe it took him an extra effort in guiding a student like me. Thank you for your patience and hard work.

I would like to acknowledge my fellow TTCRL members – Jacob Moore, Dale Fox, Fraser Jones. Special thanks goes to Jacob for doing all the hard work and letting me walk down the paved road. I wouldn't have made it without your help. Thank you Dale for being the smart one and helping me with my class homework, and Fraser for sending entertaining engineering videos. My thanks also goes to TTCRL members who have already graduated - Kyle Chavez, Joshua Anderson, John McClintic, Ellen Wilkes Smith, Gavin Packard, and Adam Vaclavik. Thank you for your help during my undergraduate years and my early graduate years. I also want to acknowledge my college friends and my neighbors, Juhie Modi and Pooja Raman, for cooking me food and letting me play with Eli (their dog).

Finally, I would like to thank my family. I wouldn't have made it this far without them.

Abstract

Evaluation of Film Cooling Superposition Method on the Suction Side of a Blade Model

Christopher Yoon, M.S.E.

The University of Texas at Austin, 2018

Supervisor: David Bogard

Film cooling is often used for turbine airfoil cooling, and there are numerous studies of the performance of a single row of holes. Typically, blades and vanes in gas turbine engines have multiple rows of holes that interact. Consequently, there is a need to develop techniques to predict film cooling performance with multiple rows of holes. One of the method is to superposition single row cooling effectiveness to predict combined effectiveness. Although there have been many studies of superposition techniques with multiple rows of cylindrical holes, there have been very few in which shaped holes were used with a typical turbine airfoil model. In this study, film effectiveness was measured on the suction side of a turbine blade model using two rows of 7-7-7 shaped holes, with pitch to diameter ratio of 6, and the two rows were more than 40 diameters apart. Measurements were made with each row operating independently, which provided the experimental data for superposition predictions. These predictions were evaluated with effectiveness measurements with both rows operational. For these combined row tests, two different upstream blowing ratios and a wide range of downstream blowing ratios were selected.

The superposition predictions were reasonably accurate when the upstream blowing ratio was high with a corresponding smaller film effectiveness downstream (due to jet separation). However, when the upstream coolant holes were operated at optimum blowing ratio with maximum film effectiveness downstream, the superposition analysis predicted film effectiveness levels slightly lower than actual levels. These results indicate that there was an interaction between jets that resulted in higher film effectiveness than what the superposition method had predicted.

Table of Contents

List of Tables

List of Figures

Chapter 1: Introduction

1.1 Film Cooling in Gas Turbine Engines

Gas turbines are widely used in power plants and aircraft engines. As a heat engine operating on a thermodynamic cycle (Brayton cycle), the efficiency of a gas turbine engine can be increased when the ratio of the combusting temperature (hot) to the ambient temperature (cold) is made larger. This is also known as the Carnot efficiency, which is the theoretical maximum efficiency of a heat engine operating between two temperatures. Since we do not have much control over the temperature of the environment, the best way to improve the efficiency of a thermal engine is to increase the temperature of the working fluid at the combustor.

Increasing the operating temperature of the combustor brings another problem. Engine components begin to lose durability when operated in high temperature and can cause meltdown when operated in extremely high temperatures. Therefore, it is crucial to develop a way to cool the engine components while keeping the operating temperature high. Film cooling is one of these active cooling methods that helps to maintain the durability of the engine components.

An extensive background of film cooling is presented in a paper by Bogard & Thole (2006) [1]. Film cooling refers to use of coolant that has passed through internal passages within blades and vanes and is then ejected through holes to the surface. An example of a blade with film cooling holes are shown in Figure 1.1. What seem like black dots on the surface of the blade are several rows of film cooling holes ejects coolant onto the surface.

Figure 1.1: An example of a gas turbine blade [2]

Film cooling holes come in many different shapes and angles. Examples of various hole geometries are shown in Figure 1.2, which is extracted from a paper by Saumweber and Schulz (2012) [3]. The most basic hole geometry would be the cylindrical hole shown in the top-left side of the figure. More complex holes have shapes, which normally involves a straight cylindrical metering hole followed by a diffuser section at the exit. Generally, shaped holes perform better than cylindrical holes on flat plate studies. Increased cross-sectional area at the exit helps to reduce the jet momentum exiting the holes, and lateral expansion of the diffuser can help lateral spreading of the coolant on the surface [4]. Depending on the circumstances, however, such as the airfoil geometry, the location of the holes, etc., certain shapes of holes can perform better than others. Therefore, it is of great interest for gas turbine engine manufacturers to find the optimal shape and flow conditions for their vanes and blades.

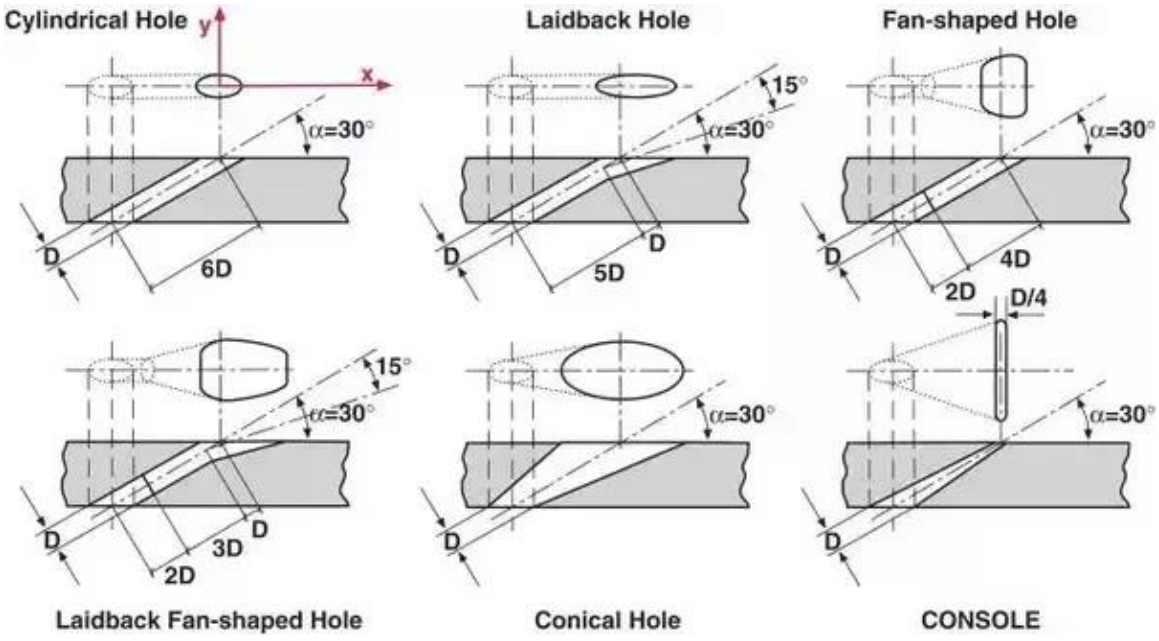

Figure 1.2: Examples of Various Shapes of Film Cooling Holes [3]

Ideally, the film of cool air stays attached to the surface, acting as an insulating layer between the wall and the hot mainstream gas. In reality, various factors play into separation or deterioration of this insulating layer. Primary factor is jet velocity, which can also be expressed as velocity ratio (VR),

$$VR = \frac{U_j}{U_\infty} \tag{1.1}$$

where U_j is the coolant jet velocity and U_∞ is the mainstream air velocity. Since coolant jets come out to the surface at an angle, if the jet velocity is too high, the coolant may separate from the surface and dissipate into the mainstream, which will result in poor

performance. On the other hand, if there is too little coolant on the surface, it won't be enough to insulate the surface far downstream.

The performance of film cooling is generally quantified using the film or adiabatic effectiveness, η, which is defined as:

$$\eta = \frac{T_\infty - T_{aw}}{T_\infty - T_c} \tag{1.2}$$

where $T_\infty$is the mainstream temperature, T_{aw} is the adiabatic wall temperature, and T_c is coolant temperature at the hole exit. The adiabatic effectiveness provides a measure of the gas temperature adjacent to the wall, which is generally considered the driving temperature for heat flow from/to the wall.

1.2 FILM COOLING IN MULTIPLE ROWS OF HOLES

Typically, there are multiple rows of holes in a gas turbine blade that interact with one another. Hence, there is a need to develop models to predict the combined effectiveness of multiple rows of film cooling holes, and one of the techniques is by superpositioning individual performance of single rows. The most widely used method was developed by Sellers [5], where the adiabatic temperature of the previous row is assumed as the driving temperature of the local temperature of a layer. For multiple (i) rows of holes, the Sellers superposition method is represented by the following equation:

$$\eta = 1 - \prod_{j=0}^{i-1}(1 - \eta_j) \tag{1.2}$$

For two rows of film cooling, the effectiveness downstream of the second row comes down to

$$\eta = 1 - (1 - \eta_1)(1 - \eta_2) \tag{1.3}$$

where η is the combined effectiveness predicted by Sellers method, and η_1 and η_2 are individual effectiveness of row 1 and row 2, respectively. In the original study by Sellers [5], injection stations had slot cooling configuration. A single-slot correlation was first obtained, and was superpositioned for multiple-slot case. Experimental data with multiple slots supported Sellers' analysis of using adiabatic wall temperature as the driving temperature of a local temperature of a layer.

The Sellers superposition model is a simplified thermal field analysis, not accounting for any hydrodynamic effects happening near the surface. Nonetheless, the Sellers model has remained a popular method of predicting combined effectiveness of multiple rows, and has been studied mostly in flat plate studies.

An insight on how upstream flow injection affects the hydrodynamics downstream can be gained by looking at the velocity field measurements by Sinha et al [6]. In this study, two rows of holes spaced 40 hole diameters apart on a flat plate were investigated. They found that for the second row, the thicker boundary layer due to the upstream injection enabled the jets to penetrate deeper into the mainstream. Since this type of hydrodynamic

effect is not taken into account by the Seller's model, the combined film effectiveness would likely be lower than what is predicted by superposition model.

Insights on how the row to row interaction affects film cooling effectiveness can be obtained from a study done by Harrington et al [7]. In this paper, 10 rows of staggered cylindrical holes with normal injection angle were studied on a flat plate. While the Sellers model predicts an increase in combined effectiveness all the way through the last row, the actual measurement showed a plateau in maximum effectiveness around the fourth row for low blowing conditions and the eighth row for high blowing conditions. Although the Sellers model worked well to the first 2-3 rows of holes, it failed to predict the effectiveness as the row-to-row interactions were degrading the overall film cooling performance. Note that in actual applications, airfoils do not have 10 rows of cylindrical holes with normal injection angle on a flat surface. What this study showed was that the superposition model may fall apart when row to row interactions are not negligible. It is not evident, however, whether just two rows with aligned holes would interact and deviate from superposition prediction.

An idea on how aligned holes in two rows behave can be gained from a computational study done by Wang et al. [8]. In this study, a numerical analysis (RANS with Realizeable k-ε turbulence model) was carried out to evaluate the Sellers superposition model with round holes and fan shaped holes on a flat plate. The upstream and downstream holes were aligned and the row spacing was ranging from 6 to 20 hole diameters apart on a flat surface. For round holes, they found that the Sellers superposition model predicted significantly higher film effectiveness than actual values when the rows were closely spaced, but predictions improved with increasing distance between rows. For shaped holes, the film effectiveness predictions by the Sellers superposition model was less

than 10% high for the 6d row spacing, with negligible error for row spacing greater than 15d. However, the results from this study should be seen with caution. Given that RANS generally gives poor predictions on film cooling effectiveness, Wang et al. validated their base cases with experimental results. However, their validation of a single round hole showed poor predictions. While the validation shown for shaped holes showed good predictions for the laterally averaged effectiveness, they did not provide the contour plots, and the blowing ratio was not stated. Also, validation of combined row performance for shaped holes was not presented. Since there were no other similar data with reliable results available for a flat plate study, this paper is referenced as a part of literature review.

The closest experimental study on a flat plate that is similar to the computational study done by Wang et al. was done by Saumweber and Schulz [9]. They conducted a comprehensive set of experiments on a flat plate to investigate interaction of film cooling rows. Two different types of hole shapes (cylindrical and fan-shaped), three configurations of streamwise spacing (10d, 20d, 30d), and a range of blowing ratios (0.5 – 2.0) for the first and second rows were tested. They evaluated superposition predictions using the Seller's model, but only for the fan-shaped holes with streamwise spacing of 10d with low blowing ratios. Furthermore, they only showed results over the range x/d = 2 to 16. In this range they concluded that superposition predictions were satisfactory in the range from x/d = 10 to 16. Note that this is a very small range. Consequently, this study provided only a very limited evaluation of the Seller's superposition model.

There are several studies that investigate the validity of Sellers superposition model on curved surface of airfoils as well. But most of them involve arrays of cylindrical holes. Anderson et al. [10] investigated closely spaced, radially oriented cylindrical holes on the leading-edge showerhead region. They found reasonable predictions at lower blowing

ratios on the suction side, but superposition predictions were significantly lower than actual values at higher blowing ratios on both pressure and suctions sides.

Predictions with the Sellers superposition model for film cooling on vane models with showerhead coolant interacting with pressure side coolant holes were investigated by Polanka et al. [11], and interactions with suction side holes by Ethridge et al. [12]. These were studies done on round holes. For low mainstream turbulence, these studies found that the superposition model predicted significantly higher effectiveness levels than the actual film effectiveness. For high mainstream turbulence intensity (Tu = 20%), the Sellers superposition predictions on the suction side of the vane worked reasonably well but were still overpredicting film effectiveness on the pressure side of the vane.

Mhetras et al. [13] studied full coverage film cooling on a blade model with six rows of shaped holes on the pressure side and four rows of shaped holes on suction side. The hole geometry was not specified, but it was indicated that the holes were compound angled. A range of blowing ratios were used with a factor of 2.7 variation in level. Single row tests showed that, for all rows, maximum performance was obtained at their maximum blowing ratio. This indicates that there was no significant separation of the coolant jets for any of the operating conditions. The Sellers superposition model was used to predict performance of the multiple row cooling with and without the showerhead operational. The superposition predictions were found to correspond well with measured values for all conditions tested. It should be noted that while using shaped holes on the suction side of the airfoil makes this paper closely related to the topic of this thesis, the holes being compound angled holes makes it very different from the experimental conditions of this thesis.

In summary, studies on flat plate suggested that Sellers superposition method worked well for shaped holes than cylindrical holes, and for holes spaced far apart than holes spaced closely together. It was inconclusive whether Sellers model generally overpredicted or underpredicted the combined effectiveness. Computational study done by Wang et al. [8] suggested overprediction, while velocity field measurement by Sinha et al. [6] suggested underprediction, although velocity field is not directly related to film effectiveness. Previous studies on airfoil models showed that superposition model overpredicted effectiveness at low mainstream turbulence when showerhead coolant interacted with pressure or suction side jets, but was more accurate for suction side at high mainstream turbulence for round holes ([11], [12]). Mhetras et al. [13] showed that for shaped holes, Sellers model worked well with and without showerhead operational, but the holes were compound angled, the information about hole geometry was limited, and the blowing ratio did not have a big enough range to observe separation.

1.3 OBJECTIVE OF THE CURRENT STUDY

For this study, experiments are conducted to study the film cooling performance for two rows of shaped holes, spaced far apart (45 hole diameters), on the suction side of a blade model. The holes between different rows are closely aligned, which would closely align the coolants from upstream and downstream rows. One objective of this study was to evaluate the performance of the Sellers superposition method on this blade model. Of particular interest were test cases in which coolant from the upstream of holes were operated at a high blowing ratio, causing significant coolant jet separation before the jets reached the downstream row of holes. The Sellers superposition model does not inherently consider the hydrodynamic effect of coolant jet separation, but the separated jet may

interact with downstream coolant jets that could improve performance by bringing some of the coolant down to the surface. Another case of interest was when the upstream jets were still attached to the surface by the time they reached second row. It was not inherently obvious whether jet to jet interactions on the surface would improve or worsen the performance after the second row than what is predicted by Sellers model.

Chapter 2: Test Facilities and Experimental Setup

2.1 Description of the Wind Tunnel Facility and Test Section

The experiments were run in a closed-loop, low-speed wind tunnel in the Turbulence and Turbine Cooling Research Laboratory (TTCRL) at the University of Texas at Austin. A detailed description of the wind tunnel facility can be found in Chavez (2016) [14]. An overall schematic of the wind tunnel facility from [14] is shown in Figure 2.1. The main fan (I) recirculated mainstream air in the direction indicated by the arrows. The recirculating air went through the main heat exchanger (J) which controlled the mainstream air temperature. Then the air went through a nozzle and accelerated to a desired approach flow velocity to the test section. After the test section and before the main fan, some of the mainstream air was extracted (A) and entered the coolant loop (B).

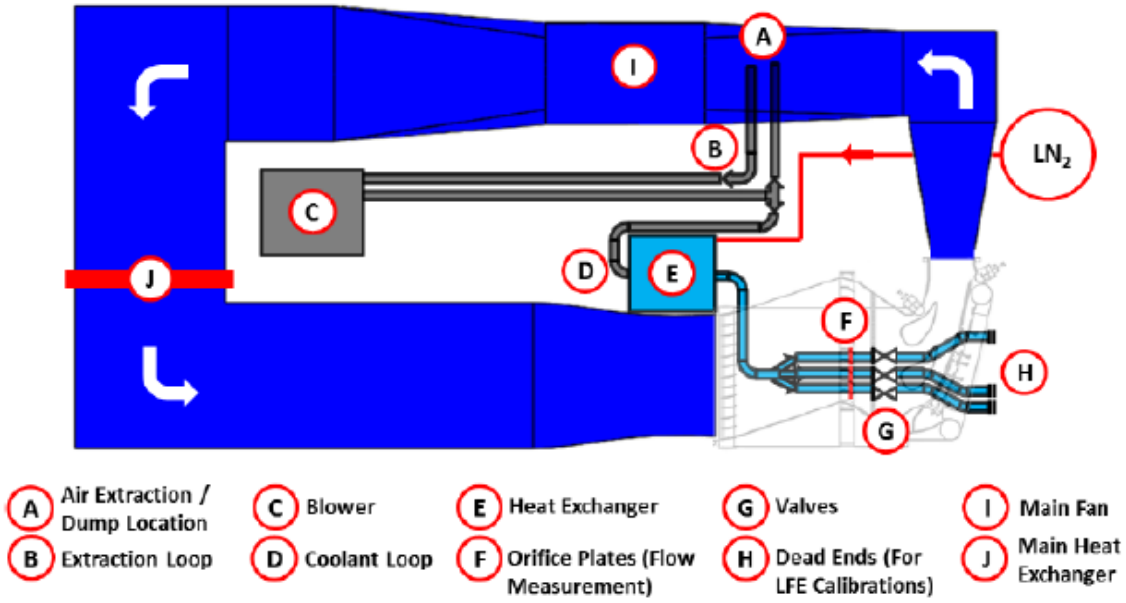

Figure 2.1: Schematic of Recirculating Wind Tunnel with Incidence Angle of 0° [14]

A secondary blower (C) was used to drive the coolant loop. Part of mainstream air drawn into the secondary blower was mixed with liquid nitrogen in the coolant heat exchanger (E). The coolant flow out of the heat exchanger was split to two pipes (D) that were connected to two internal plena of the blade model. Each pipe had valves (F) that could control individual flowrate. Although the diagram shows three valves, only two of them were used for this study.

Two coolant pipes were attached to each plenum inside the blade model. By controlling the flowrate of each pipe with a valve, the desired blowing ratios were met. As it will be explained later in Chapter 3, having different flowrates for each pipe led to having different temperatures, since different amount of coolant compensated for heat influx through the valves. One way to correct this and maintain same temperature for both plena was to use both of the two valves for each pipe to increase/decrease heat influx from the surrounding environment. However, in an extreme case where there was still considerable temperature difference between plena, the test result was omitted from the data set.

A schematic of the test section of the wind tunnel is shown in Figure 2.2, a figure taken from [14] with updated blade geometry by Moore (2018) [15]. Before entering the test section, the mainstream flow went through two stages of turning vanes and approached the blade model with an angle of attack. The intended approach angle was 35° to the axial direction, which around the nominal design for this blade (31.1°). Previous to this study, Moore (2018) [15] had run experiments investigating the single row effectiveness in low turbulence condition. In his study, the actual approach angle was found to be 33.7°.

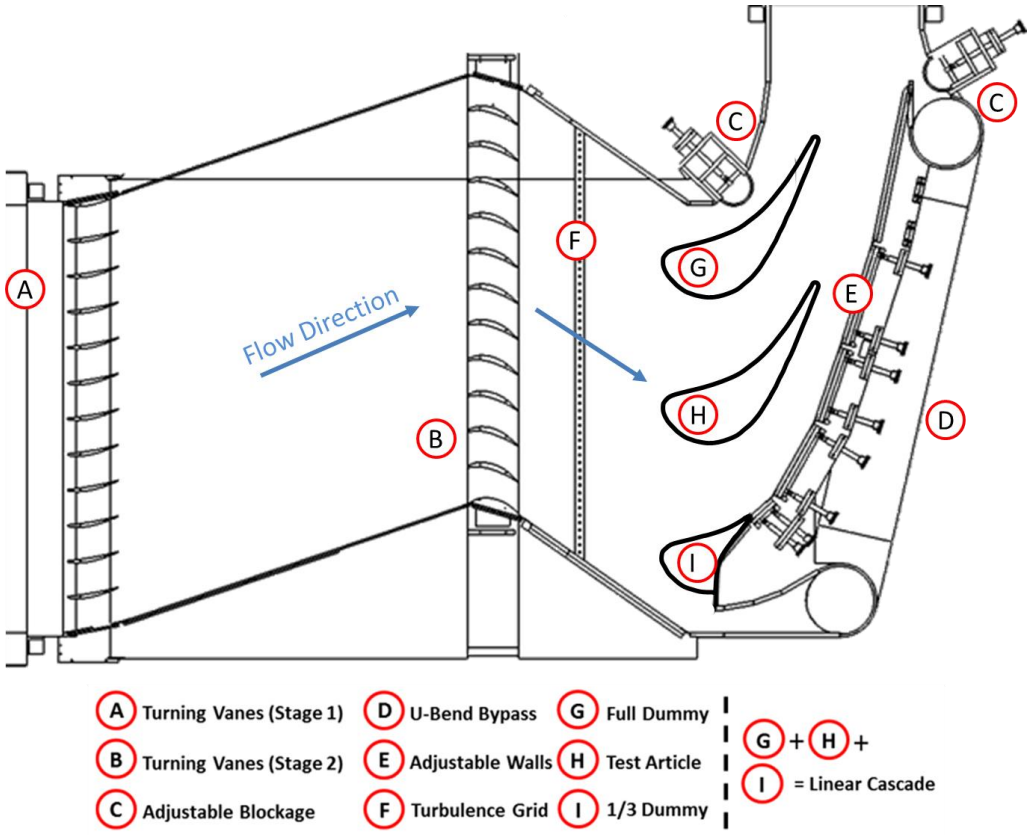

Figure 2.2: Top-Down view of the Test Section with Current Blade Model (From [15], adapted from [14])

In the test section, the test model (H) was located in the middle while dummy blades comprised the remainder of the linear cascade simulating the periodic boundary conditions. The bypass passages (C and D) and adjustable side walls (E) were adjusted to match the desired stagnation line location and the pressure distribution along the test model and the dummy models.

As mentioned previously, Moore (2018) [15] had run experiments in the same wind tunnel facility with the same blade model. In this study, all test conditions were identical

to those of [15], such as the approach and exiting velocity, mainstream temperature, blade geometry, pressure coefficient (C_p) distribution, and the coolant parameters. Thus, test setup described in this thesis summarizes what is already presented in [15]. The only difference in test condition was the presence of the turbulence grid (F) for this study. This created high turbulence level in the mainstream as intended, but it also changed the approach angle of the flow from 33.7° to 26.5°. A more detailed description of the turbulence grid will be discussed in the next section, *2.2 Description of the Turbulence Grid*. A simple summary of experiment setup is presented in Table 2.1. Note that the chord Reynolds number was matched to engine conditions.

Table 2.1: Mainstream Flow Conditions for this study

Parameter	Value
Inlet Velocity	6.38 m/s
Exit Velocity	16.75 m/s
Inlet Angle	-26.5°
Exit Angle	70.7°
Mainstream Temperature	303K
Approach Turbulence Intensity at $0.2C_{AX}$ upstream	18%
$Re_{C,\ inlet}$	240,000

2.2 DESCRIPTION OF THE TURBULENCE GRID

As mentioned in the previous section, the presence of turbulence grid makes this test condition different from [15] which studied cases with low mainstream turbulence. An image of the turbulence grid is shown in Figure 2.3.

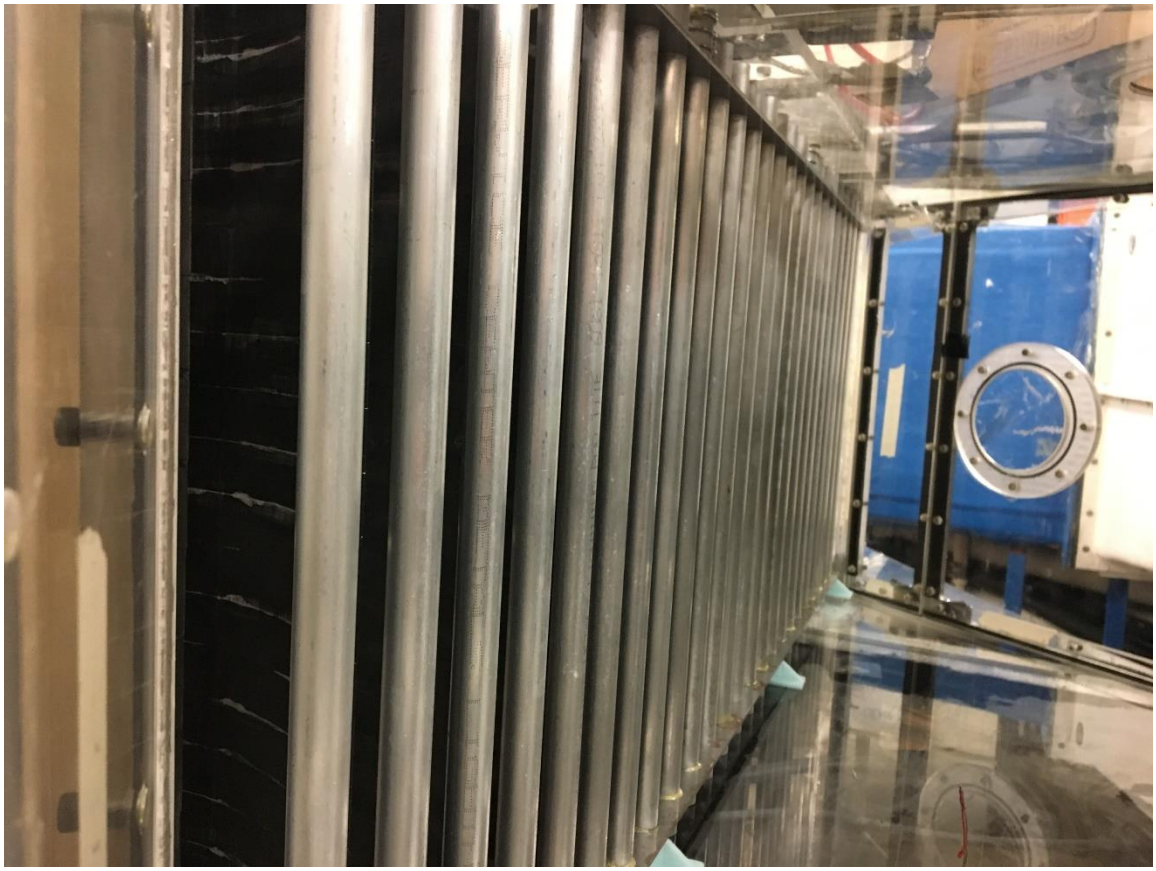

Figure 2.3: Image of the Turbulence Grid Setup

In the design phase, the target was to have around Tu = 15% at $0.2C_{AX}$ (axial chord length of the blade) upstream of the geometric leading edge of the blade, in the axial direction. Turbulence intensity is defined as follows:

$$Tu(\%) = \frac{u_{rms}}{U_{mean}} \tag{2.1}$$

where U_{mean} is the time average flow velocity and u_{rms} is the root-mean-square of fluctuating velocity component with respect to the mean velocity. For this wind tunnel facility, there was already a study done by Packard (2015) [16] that investigated turbulence decay downstream of the grid. Given that there was not much space in-between the desired turbulence measurement location and the second stage of turning vanes, the author used the data by Packard to find the appropriate bar diameter to generate desired turbulence intensity. The target value and the measurement location of turbulence intensity are shown in Figure 2.4 and Figure 2.5.

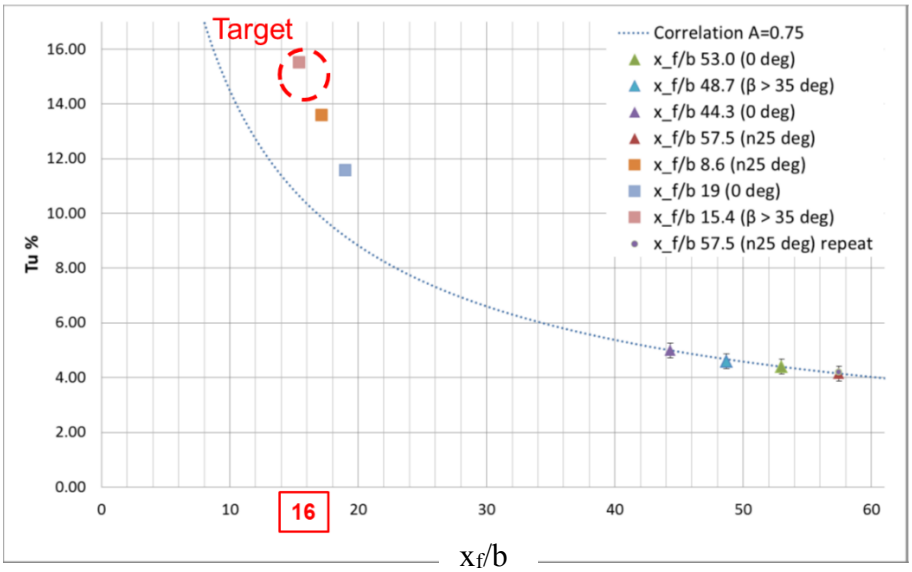

Figure 2.4: Decay of turbulence downstream of bar grid, based on Packard (2015). (x_f : Flow Distance, b : Grid bar diameter). The target of Tu = 15% is shown on plot.

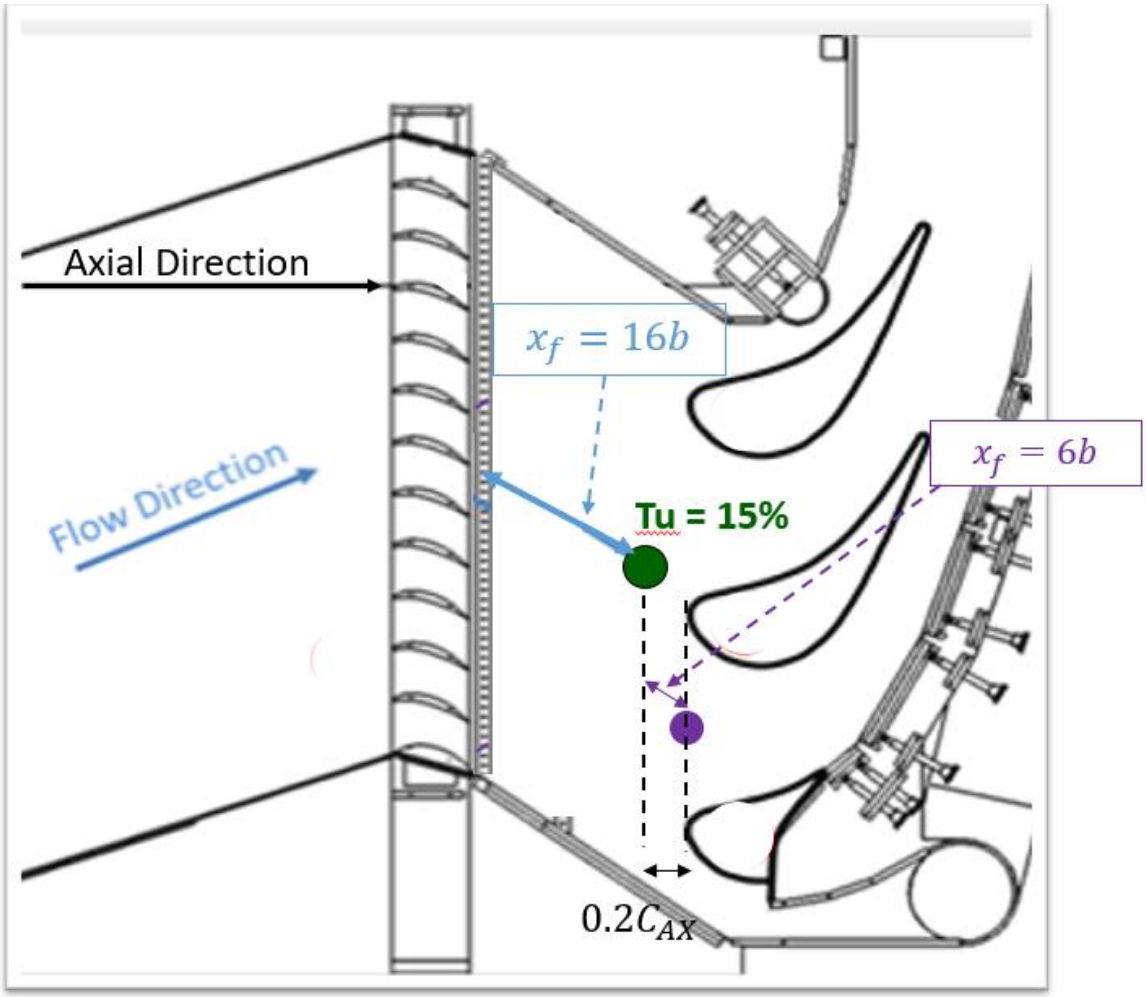

Figure 2.5: Targeted Turbulence Intensity and the Measurement Location (Distances not to scale)

Figure 2.4 shows measurements of turbulence decay downstream of the bar grid with varying flow angles, from 0 degrees to 35 degrees, in the same wind tunnel facility. The correlation between the turbulence intensity (Tu) and the flow distance (x_f) normalized by bar grid (b) is shown in the figure as dotted lines, where $Tu = A * \left(\frac{xf}{b}\right)^{-\frac{5}{7}}$, a correlation initially developed by Roach [17]. The constant A that Packard used was 0.75. As it can be seen from the figure, some data set do not agree well with this correlation, so deciding

whether to use this correlation was based on the target. Since the target was Tu = 15%, Packard's data indicated that $x_f/b = 16$ (where x_f is the flow distance and b is the grid bar diameter) was needed to achieve the target Tu = 15% at the location. Figure 2.5 shows the grid position relative to the blade model and the turbulence measurement location. With this constraint, the aluminum rods for the turbulence grid had a diameter of 0.75 inches. The grid had a pitch of 1.67 inches, which created a solidity of 45%. Since the flow angle was around 35 degrees, the effective solidity was around 55%.

Although the target was to achieve Tu = 15% at that location, the actual measurement using hot wire probe showed that the average turbulence intensity was slightly higher, around 18%. The plots showing turbulence intensity in the spanwise distance at $0.2C_{AX}$ upstream is presented in Figure 2.6. Due to the limitation of the length of the hot wire probe holder, a full measurement of one pitch could not be achieved on the pressure side. There were some span-wise variation in turbulence intensity, but note that the turbulence seen along the suction side wall would be the turbulence level measured slightly to the suction side of the stagnation line (y = 0). Coincidentally, the average turbulence intensity matches with the turbulence seen by the suction side of the blade, both being Tu = 18%.

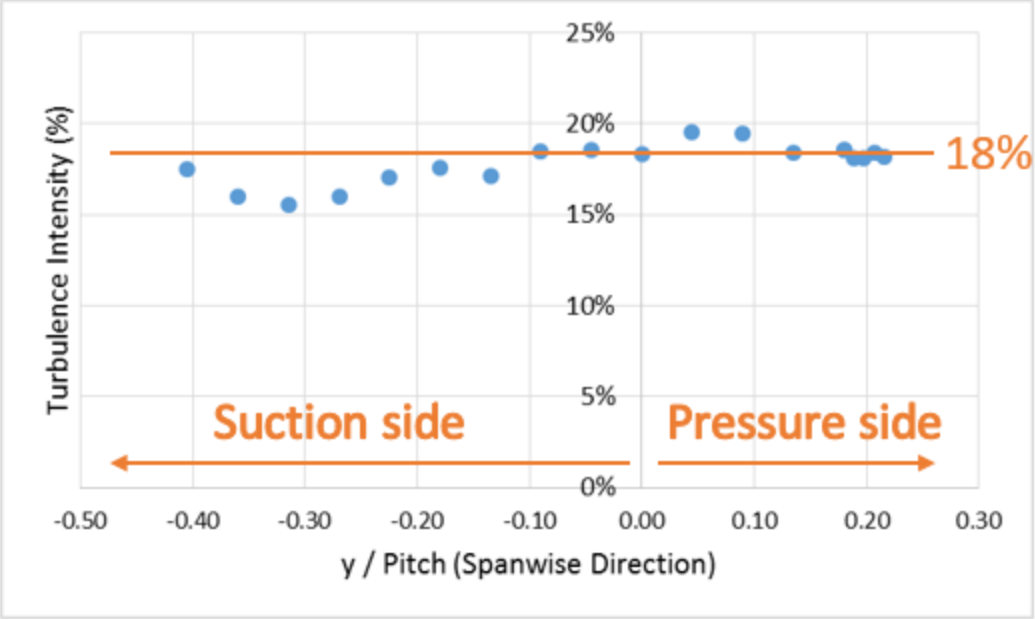

Figure 2.6: Spanwise Measurement of Turbulence Intensity (Pitch : Spacing of the blade models)

Although the wall orientation upstream of the blade model has remained the same, the presence of the turbulence grid changed the incoming flow angle. Chavez (2016) [14] provides a correlation for flow angle after the turbulence grid is given as follows:

$$\beta_{out} = -13.32 + 5.177 \times 10^{-1}\beta_{in} + 8.103\left(\frac{p_{bar}}{D_{bar}}\right) + 1.8 \times 10^{-3}\beta_{in}^{2} + 0.0678\beta_{in}\left(\frac{p_{bar}}{D_{bar}}\right) - 1.111\left(\frac{p_{bar}}{D_{bar}}\right)^{2} \quad (2.2)$$

where β is the flow angle before or after the grid, p is the pitch and D is the diameter of the bar. According to this correlation, the turbulence grid is predicted to change the incoming mainstream flow angle to 27.5° from 33.7°. Using Particle Image Velocimetry (PIV), it

was confirmed that the flow angle is around 26.5°, significantly different from low turbulence case. Therefore, the side walls of the test section had to be adjusted to match the C_p distribution.

2.3 Description of Kopriva Blade Model and Hole Geometry

The geometry of the blade model was taken from a numerical study by Kopriva et al [18], and the blade is referred as "PBD01" in the paper. A detailed analysis of geometric scaling and flow scaling was performed by Moore (2018) [15], but a summary will also be presented here.

The pitch-to-chord ratio p/C was given as 0.739, where p is the blade pitch and C is the blade chord length [18]. Since the wind tunnel used for this experiment fit a minimum pitch of 445mm, this resulted a scaled-up chord size of 602.3mm. In terms of flow scaling, the Reynolds number of blade chord length was 240,000 for the inlet and 510,000 for the outlet. When the mainstream air is operated at 303K, which is the nominal operating temperature of this wind tunnel, this yielded the inlet velocity of 6.38 m/s. This is summarized in Table 2.1 in Section 2.1. One interesting aspect of the flow scaling was that although this was a flow condition with low Mach number, the C_p distribution simulated a high Mach number case.

For this study, two rows of holes were used on the suction side of the blade model. The upstream row (Row 1) was placed at s/C = 0.334, which corresponded to a region with high surface curvature. The downstream row (Row 2) was placed at s/C = 0.798, a relatively flat region of the blade.. Here, s indicates streamwise distance from the geometric leading edge, and C indicates the chord length of the blade model. The radius of curvature

(R) normalized by the hole diameter(d) was 2R/D = 56 for the high curvature region and 213 for the low curvature region. A 3mm diameter trip was placed ahead of the upstream row to force a desired boundary layer thickness at row 1. The location of the trip and two rows of holes are shown in Figure 2.7.

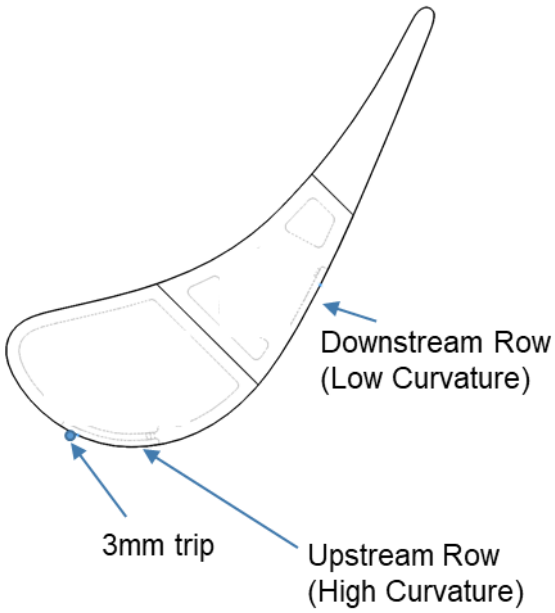

Figure 2.7: Schematic of Blade Model Geometry and Hole Locations

Like the blade model, the holes used in these experiments were the same ones presented in [15], based on the 7-7-7 shaped hole design presented in Schroeder and Thole (2014) [19] with 7° forward and lateral expansion angles. The standard geometry is also shown in Figure 2.8. However, as described in [15], slight modifications to the design had to be made since the shaped hole was placed through a curved wall. While the standard 7-

7-7 hole geometry has AR of 2.5, row 1 and row 2 had AR of 2.44 and 2.48, respectively. The hatch thickness scaled by hole diameter (H/d) is 3 for standard hole geometry, and 2.34 and 2.94 for the row 1 and row 2 holes.

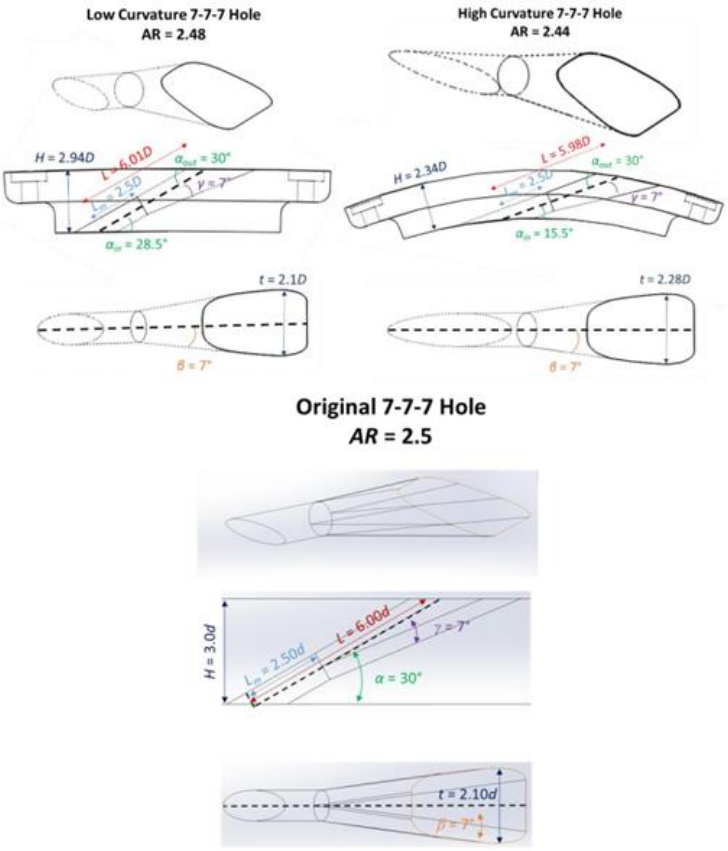

Figure 2.8: 7-7-7 Hole Geometry [15]

It is important to note that the diameters of the inlet metering sections for each row was slightly different – 6.09mm for row 1 and 5.6mm for row 2. This was done to keep the hole Reynolds number constant around Re_d = 6,700 for both rows of holes, which was

similar to the hole Reynolds number from many tests performed on the standard 7-7-7 hole in TTCRL's flat plate facility. Since the flow accelerated on the suction side, higher velocity at the second row resulted in smaller hole diameter. The spacing between holes was kept at P/d = 6, where P is the pitch, causing slightly different spacing for each row of holes, resulting in slightly staggered position of holes for row 1 and row 2. However, each row was symmetrical to the centerline of the blade span, and the measurements were made for the middle two holes. So the difference in hole spacing did not propagate more than once, meaning that these holes were the best aligned holes among all holes of the two rows. Table 2.2 shows hole parameters for both rows of holes.

Table 2.2: Hole Parameters

Parameter	Row 1	Row 2
Hole Type	7-7-7	7-7-7
Hole Position (s/C)	0.334	0.798
Diameter of metering hole (d)	6.09 mm	5.6 mm
Local Velocity	15 m/s	16.7 m/s
Hole Reynolds Number (Re_d)	6600	6800
Pitch to Diameter Ratio (P/d)	6	6

2.4 Description of Instruments and Calibration

Four infrared (IR) cameras were placed along the suction side of the blade model to read temperature contours along the surface of the blade. The surface of the blade was painted black to maximize emissivity. Salt crystal windows and a zinc-selenide window

were used to allow infrared-range optical access for these IR cameras. The position of the IR cameras, as well as the hole locations are shown in Figure 2.9. For each test condition, all four cameras took 5 images each, and the images were averaged for final processing. The overlapping region was processed with a linear weighing function, so that two images blended together well. A more detailed description of the IR camera calibration is discussed in [15].

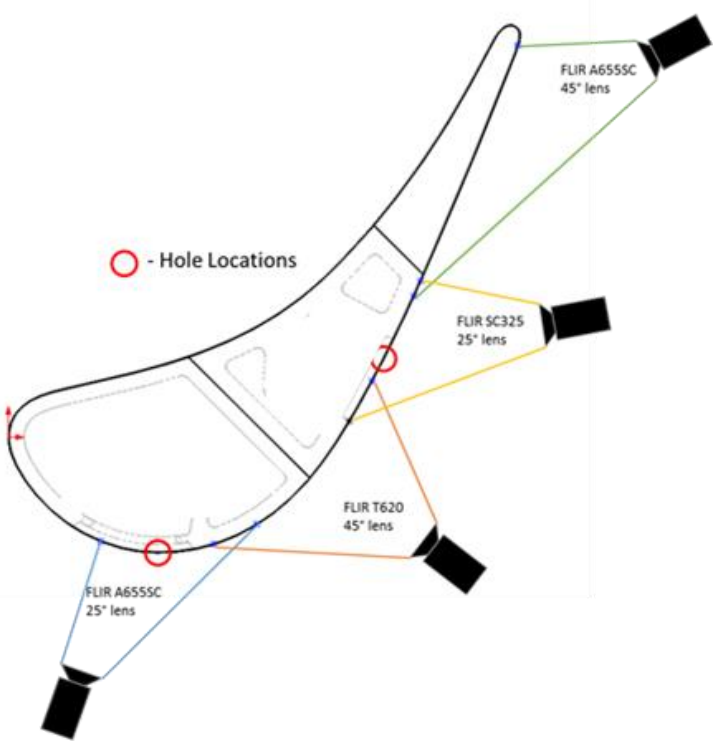

Figure 2.9: Schematic of IR Cameras and Hole Location

The only outlet for the coolant air inside the blade was through the row of film cooling holes into the mainstream, which simulated a plenum feed commonly used in flat plate film cooling studies. The decision to use plena for this model was based on a desire

to minimize the effects of cross-flow of coolant on the film cooling performance. The cross-flow in typically internal channels used in turbine blades can significantly alter film cooling performance [20].

Four calibrated thermocouples were placed in each plenum at the exit of the holes, to measure the average the coolant temperature exiting the holes. Three thermocouples were placed in the mainstream to measure the average mainstream temperature. These two temperatures of coolant and mainstream were used to calculate the density ratio. Throughout the experiment, the coolant to mainstream density ratio (DR) was maintained at 1.20.

Pressure transducers were connected to orifice plates of coolant pipes to monitor coolant flowrate, and to a Pitot static probe placed at the exit of the suction side to measure velocity. The reason for measuring the exit velocity was because CFD simulation done in the lab indicated that the flow velocity is relatively uniform at the exit. Monitoring coolant flowrate is important because it helps to detect frosting in the coolant pipes and holes. Frosting is an issue often encountered when coolant is run at 250K for several hours that eventually blocks a significant portion of coolant flow. Seeing frosting occurring ahead of time and preventing it allows for accurate measurement of hole effectiveness. The exit velocity measurement ensures that the mainstream velocity is at steady state, staying within the intended range of acceleration through the suction side. Calibration of pressure transducer, thermocouples and IR cameras, as well as the uncertainty calculations are explained in [15].

2.5 TESTING PROCEDURES AND DATA PROCESSING

For all film cooling tests in this study, the density ratio (coolant density to mainstream density) of DR = 1.20 was maintained throughout the experiment by cooling the coolant air to about 250K using liquid nitrogen. When the measured temperature showed a slight difference between row 1 and row 2 coolant, row 2 was prioritized to match the density ratio. A range of coolant blowing ratios was used for rows 1 and 2 by adjusting the flowrate for each coolant pipe.

To apply the Seller's superposition method, data with individual row measurements was first collected. Blowing ratios of M = 1.0 to M = 3.0, in 0.5 increments, were conducted for each row and adiabatic effectiveness was measured. The blowing ratio M is defined as follows:

$$M = \frac{\rho_c U_c}{\rho_\infty U_\infty} \tag{2.3}$$

where ρ_c and U_c are coolant density and velocity at the metering hole, and ρ_∞ and U_∞ being mainstream air density and local velocity. To find U_c, the measured mass flow rate of the coolant through the pipe was divided by the number of holes, the density of the coolant from temperature measurement, and the area of the hole. U_∞ came from the C_p value at the location measured by [15].

To apply conduction correction, two holes were blocked to get an approximate measurement of 1-D conduction effect through the walls. The adiabatic effectiveness measured with two center holes blocked is termed η_0. Note that η_0 is only measured along the centerline in-between the blocked holes and is a function of stream-wise coordinates. The correction was assumed to be constant in the span-wise direction.

After η_0 values are obtained, conduction correction is performed. The correction method comes from heat transfer analysis in Appendix C of *Robertson (2004)*. The corrected adiabatic effectiveness is found as follows:

$$\eta_{corrected} = \frac{\eta_{uncorrected} - \eta_0}{1 - \eta_0} \tag{2.4}$$

Figure 2.10 shows example plots of η_0 and corrected and uncorrected $\bar{\eta}$ (laterally averaged effectiveness) of row 1 at three different blowing ratios. Although η_0 values were obtained at each blowing ratio, the η_0 level did not vary much with blowing ratio. This is consistent with observation from [15]. Thus, only one plot of η_0 is shown in Figure 2.10 for clarity.

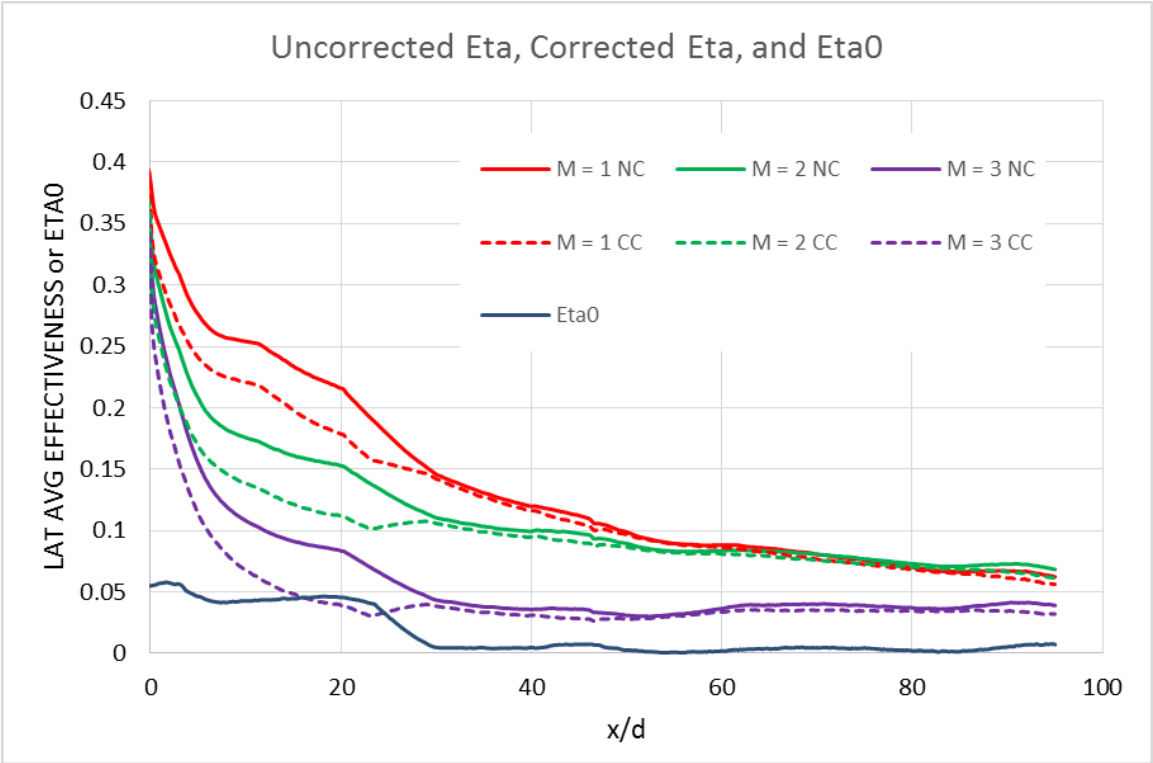

Figure 2.10: $\bar{\eta}_{uncorrected}$, $\bar{\eta}_{corrected}$, and η_0 of row 1 at various blowing ratios (NC: Not Corrected, CC: Corrected)

As it can be seen from Figure 2.10, η_0 has relatively higher values (~ 0.05) close to the hole, where the plenum is still underneath the surface. When the inner geometry changes and is not affected by coolant anymore, η_0 level is close to zero. The relative magnitude of η_0 depends on the effectiveness. At x/d = 20, where the correction is maximum, the correction ranges from 20% to 50% of the uncorrected effectiveness value, depending on the blowing ratio M.

With corrected adiabatic effectiveness for individual rows, Sellers superposition method was used to predict the combined row effectiveness downstream of the second row. Next, the actual combined effectiveness with both rows operating were measured.

For combined row experiments, both row 1 and row 2 were operational for a range of blowing ratios from M = 1.0 to M = 3.0. To reduce the test matrix, two upstream blowing ratios of M_1 = 1.5 and 3.0 were selected, with the selection criteria explained in Chapter 3. With two upstream blowing ratios (1.5, 3.0) and five downstream blowing ratios (1.0 – 3.0), the effectiveness were measured in the same condition as single row experiments except that both rows were running. For conduction correction, two holes were blocked for each row, and η_0 measurements were made with both rows operational to find η_0. The corrected effectiveness were then compared with superposition predictions.

The most straightforward way to compare the effectiveness levels between superposition method and actual measurement is to look at effectiveness contours. However, when the contours don't show definite differences, laterally averaged effectiveness ($\bar{\eta}$) are used to compare the effectiveness levels. $\bar{\eta}$ is simply effectiveness averaged over two pitches in lateral direction on the surface.

2.6 UNCERTAINTY ANALYSIS

A summary of the uncertainty of the measurements is presented in this section. Uncertainty was propagated via sequential perturbation method. Each instrument had bias and precision uncertainties. Precision uncertainty was minimized by taking many data points at each setpoint measurement. For temperature measurements by thermocouples, data rate of 350Hz was used, and 700 samples were taken for each measurement point. Five of these 700 measurements were averaged together for the measurement point, further reducing the precision uncertainty. A more detailed analysis of uncertainty as well as calibration procedures for various instruments are outlined in [15].

Uncertainty in Pressure

Depending on the pressure transducer model and its range, the uncertainty δP ranged from 0.28 Pa to 13Pa. The percentage uncertainty at typical reading ranged from 0.2% to 2.5% for the transducers used in this study. This came from the calibration of transducers using a micromanometer. The uncertainty from curve fit was determined using the following equation [21]

$$\delta y(x_p) = \pm t_{\alpha/2\,,n-2}\, s_{y,x} \sqrt{\frac{1}{n} + \frac{\left(x_p - \bar{x}\right)^2}{SS_{xx}}} \tag{2.5}$$

where δy is the uncertainty in calibrated value y, $t_{\alpha/2\,,n-2}$ is the t-distribution of the calculation with n-2 degrees of freedom using 95% confidence interval, $s_{y,x}$ is the standard error of the estimate, n is the number of calibration points, x_p is the x-coordinate sample in the calibration, $\bar{x}$ is the mean of the x-coordinate samples, and SS_{xx} is the sum-of-squares

of x-coordinate deviations from the sample mean. In the case of pressure transducer calibration, x is the voltage reading and y is the resulting pressure in Pa. Pressure transducers' zero drifts were no more than 10% of the calculated calibration uncertainty and was not accounted for [15].

Uncertainty in Temperature Measurements, Density Ratio, and Blowing Ratio

Thermocouples were all calibrated in the glycol-water bath at the same time. Note that the reference temperature of the bath has been previously measured by Kistenmacher [22] with a NIST traceable Fluke temperature meter with a thermistor probe. The temperature of the bath was found to be within the uncertainty of the meter/probe pair, $\delta T = 0.013$ K, and found to be uniform to within $\delta T = 0.006$K at various points in the bath. Therefore, the uncertainty in the reference bath temperature is limited by the accuracy of the meter, 0.013K. Chavez [14] noted that it had been two years since that calibration, and the 0.05K was utilized recognizing that this was a conservative estimate of the uncertainty, and this thesis follows the same reasoning. Precision uncertainty was less than 0.01K based on the standard deviation of the temperature measurements. Most of the bias uncertainty came from the uncertainty in the calibration. The average standard error of the thermocouple calibrations was 0.09K.

For measurements of mainstream temperature and coolant temperature, several thermocouple measurements were averaged together. A spatial uncertainty was estimated for these averaged temperatures. This was found to be about 0.2K for T_∞ and 0.3K for T_C. Since this was a low Mach-number flow, the ratio of pressures of the coolant and the mainstream were assumed to be unity. As a result, the density ratio is simply

$$DR = \frac{\rho_c}{\rho_\infty} = \frac{T_\infty}{T_{c,exit}} \tag{2.6}$$

And the propagation of uncertainty yields δDR = 0.002. This was much smaller than the range of acceptable DR values that the operator used as a guideline, which was DR = 1.20 ±0.005.

The blowing ratio from directly measured quantities is shown as the flowing equation

$$M = \left(\frac{\beta * d_{pipe}}{D}\right)^2 \left(\frac{C_d}{N_{holes}}\right) \sqrt{\frac{\Delta P_{orifice}}{\Delta P_{outlet}} * \frac{P_{orifice,abs} T_\infty}{P_{static,outlet,abs} T_{orifice}} * \frac{1}{1-\beta^4} * \frac{1}{1-C_{p,outlet}}} \tag{2.7}$$

where N_{holes} is the number of holes for the given row, ΔP_{outlet} is the pressure difference measured by the Pitot-static probe at the outlet, $P_{orifice,abs}$ is the absolute pressure of the orifice plate, $P_{static,outlet,abs}$ is absolute static pressure of the blade outlet, and β is the diameter ratio of the orifice plate. The uncertainty in β according to the manufacturer was very small, in the order of 0.01%. The diameter of the pipe is 3.068" ± 0.01". The diameter of the film cooling holes, D, is 6.09mm for row 1 and 5.60mm for row 2, with uncertainty of ± 0.003". N_{holes} is 10 for row 1 and 12 for row 2. The calibration uncertainty of the orifice plates was $\delta C_{d,\ calibration}$ = 0.004 for row 1 and 0.002 for row 2. The resulting uncertainty in blowing ratio was around δM_1 = 0.04 for M_1 = 1 and δM_1 = 0.10 for M_1 =

3.0 for row 1. For row 2, it was around the same: $M_2 = 0.97 \pm 0.03$ and $M_2 = 3.0 \pm 0.10$. For both rows of holes, the uncertainty percentage of blowing ratios remained around 3.3-3.5%.

Uncertainty in Adiabatic Effectiveness

To calculate adiabatic effectiveness, it was required to find three temperatures: mainstream temperature (T_∞), coolant temperature ($T_{c,exit}$), and the local adiabatic wall temperature (T_{aw}). The mainstream and coolant exit temperatures were measured by thermocouples, and relevant uncertainties have already been quantified. The adiabatic wall temperature was measured by IR cameras.

When calibrating IR cameras, surface thermocouples were attached to copper tabs. These tabs were painted black and were attached to various locations on the surface of the blade, with surface thermocouples facing the mainstream air. Since copper has high thermal conductivity, the measured temperature via thermocouples were assumed to be the average temperature of the small area in the center of the tab seen by an IR camera. An example IR calibration image is shown in Figure 2.11.

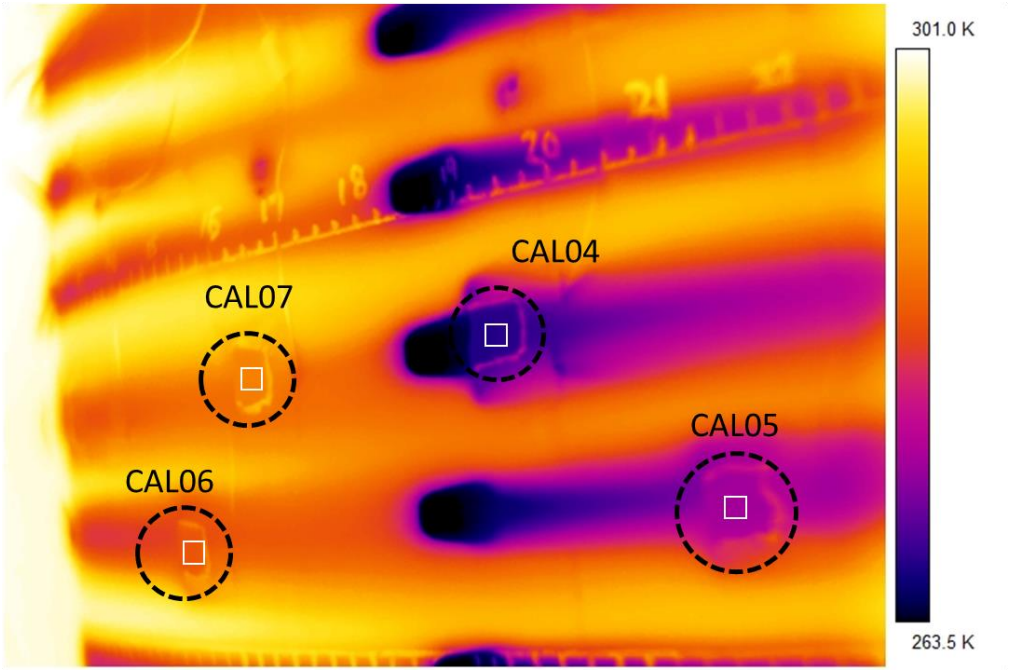

Figure 2.11: Example image of IR Calibration Process for Camera 3 (FLIR SC325). White squares indicate the small area used for finding average temperature around each surface thermocouple.

As it can be seen, there were several calibration tabs seen by one camera. This is because there is a spatial dependency of IR temperature readings, causing different calibrations for thermocouples for a given camera depending on the viewing angle. The placement of calibration coupons were arranged so that they would cover extreme range points for all cameras. Consequently, there would be a tab in the overlap region between each camera's viewing area. For example, camera 3, image shown in Figure 2.11, saw four calibration tabs - CAL04, CAL05, CAL06, and CAL07. CAL06 was also seen by camera 2 that views upstream of the area viewed by camera 3. CAL05 was also seen by camera 4 that views downstream of the area viewed by camera 3. Placing calibration tabs in these locations allowed to a spatial calibration as well as temperature calibration for each camera, and the calibration tabs located at the overlapping area would force the calibrated

temperature between cameras to be the same. Figure 2.12 shows examples of calibration curves for each camera for different calibration coupons.

Precision uncertainty in IR temperature was around 0.1K. The bias uncertainty came from calibration of IR cameras. The calibration uncertainty was conservatively taken as the maximum standard error of estimate from all the cameras, which was 0.10K. The precision and bias uncertainties propagated to uncertainty of $\eta_{uncorrected}$and η_0, which were then combined to find overall uncertainty for η. For each row, at nominally high effectiveness value of η = 0.650, δη was 0.012. At low effectiveness value of η=0.100, δη was 0.015 [15].

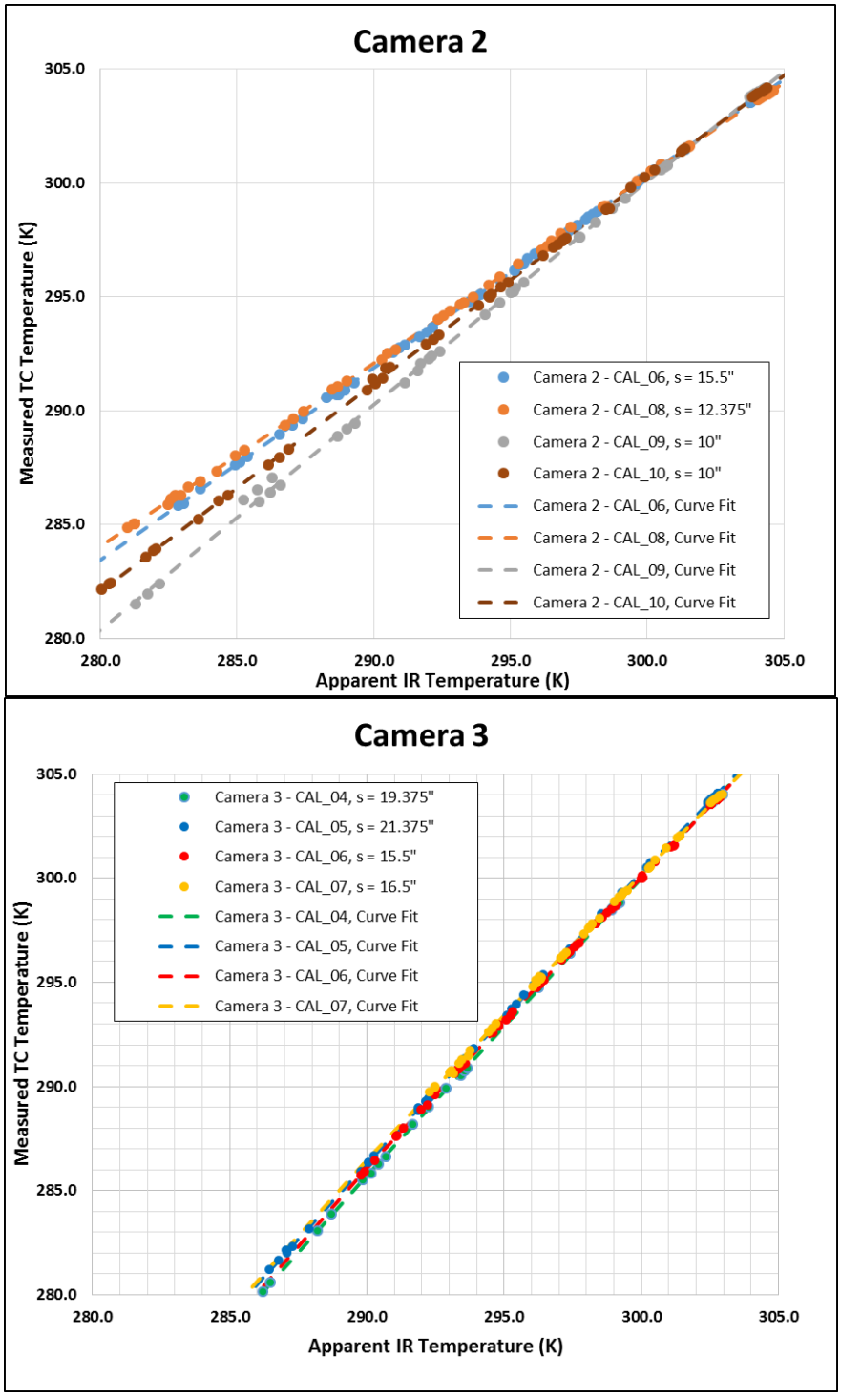

Figure 2.12: Calibration Curves for Camera 2 and 3 at Various Locations

There were many complications when performing far-field measurements on a curved surface. As mentioned previously, four infrared (IR) cameras are used to read surface temperature of the blade model, and they were calibrated with calibration tabs at various locations, including overlapping areas. Complications arose when the cameras saw different temperature in overlap region, despite going through the calibration process. An example of this case can be seen from Figure 2.13 (a), showing the laterally averaged effectiveness of a single row test for row 1 at $M_1 = 1.5$. As it can be seen, the cameras doesn't agree well in the overlapping regions. In cases like this, the effectiveness was "blended" with a weighing function. Based on the proximity to each camera in the overlapping region, the function linearly weighed each camera accordingly and interpolated the different temperature values. This method was previously used from Chavez (2016) [14], with a linear blending function of the following form:

$$D_{blended} = D_{left}(1 - \psi) + D_{right}\psi \tag{2.8}$$

where ψ represents the percent distance across the spatial distance to be blended, and D represents some type of 2D data (such as temperature or effectiveness) in the coordinate plane. This allows for the generation of a continuous dataset over the overlapping regions between cameras The resulting laterally averaged plot is shown in Figure 2.13 (b).

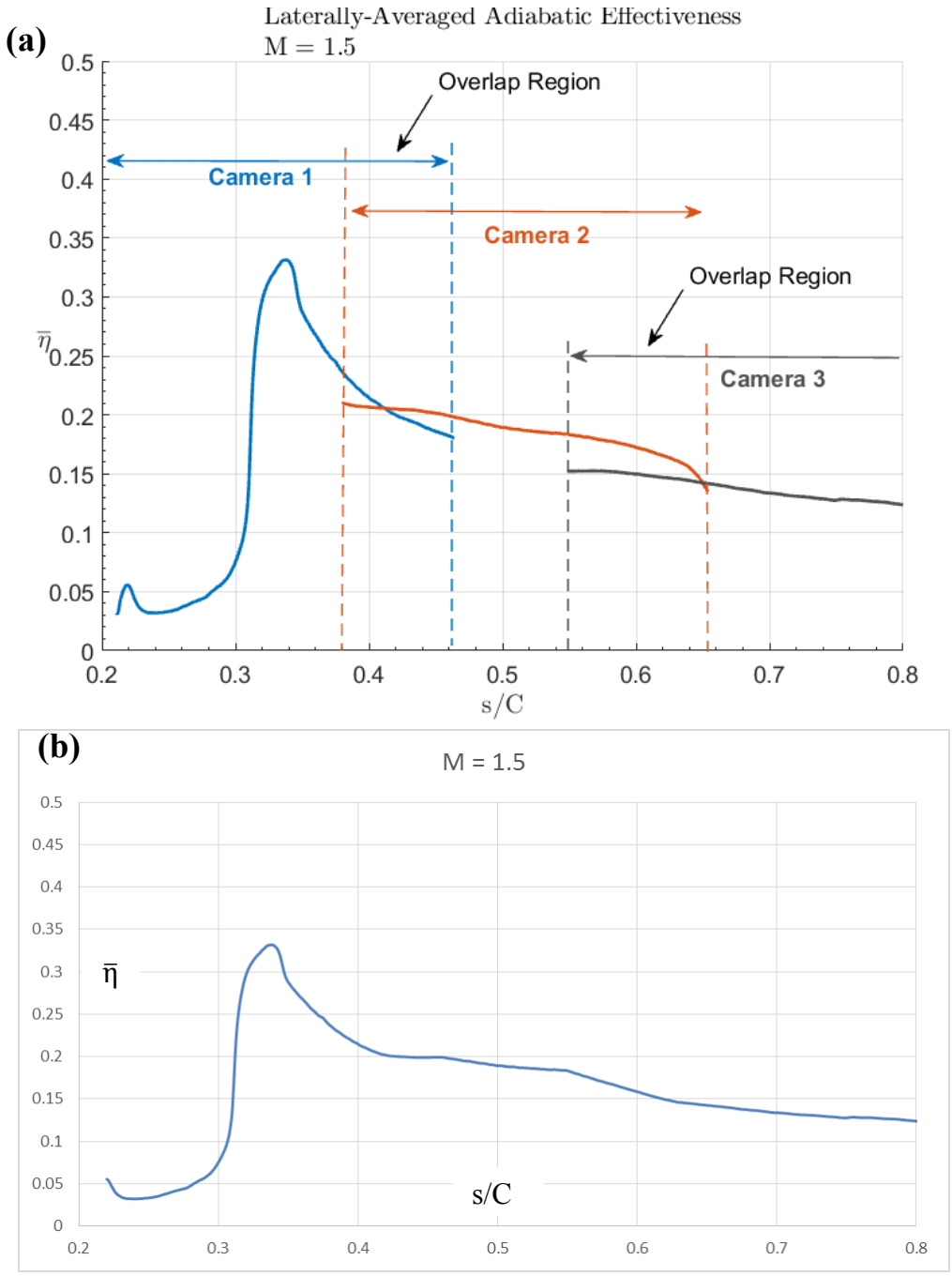

Figure 2.13: Calculations of $\bar{\eta}$ from Camera 1, 2, and 3 Measurements. (a) shows the values before interpolation. (b) shows after interpolation.

The author was not able to find a good answer on why this disagreement occurred. One hypothesis was that the angle was too shallow at the edges of viewing angle of each camera, that made measurements unreliable. Another hypothesis was that the reflections from downstream coolant could affect the upstream camera readings, and vice versa. Since we operated both rows for calibrating all four cameras, the test conditions for single row tests were not identical to the calibrating test.

Another complication arises from discontinuous internal geometry of the blade model. When there is a sudden change from air gap to foam structure, there is a complex 3-D conduction effect that is not fully corrected in 1-D conduction correction method. Quantifying the uncertainty in the overlap region is outside the scope of this thesis. More investigation is needed to understand what is affecting the different temperature seen at the overlap region.

Chapter 3: Low-Speed Blade Testing Results

This chapter is comprised of test conditions, experimental results of single row and two rows experiments, and comparison with superposition predictions. Mainstream approach flow conditions and blowing conditions for each row of holes will be presented first. Then, distributions of $\bar{\eta}$ will be presented for the single row performance for rows 1 and 2 to provide reference cases. Film cooling effectiveness for both rows combined will then be presented, and finally comparisons with Sellers superposition prediction model will be made.

3.1 TEST CONDITIONS

The mainstream flow properties and coolant flow conditions used in this study were summarized in Table 2.1 and Table 2.2. As a reminder, the summary of test conditions are presented again in Table 3.1. The approach velocity of 6.38m/s was selected to match typical operating Reynolds numbers for this blade. The turbulence grid generated turbulence levels of Tu = 18% at $0.2C_{AX}$ upstream of the blade leading edge. On the blade model, upstream of the first row breakout location, a 3mm-diameter trip was placed in order to force a boundary layer thickness of δ/d_1=1.1 at the upstream row breakout location. The trip was present in both for single row experiments and two row experiments.

Table 3.1: Operating Conditions

Mainstream Temperature, T_∞	303 K
Approach Velocity, U	6.38 m/s
Exit Velocity, U	16.75 m/s
Turbulence Intensity, Tu (at $0.2C_{AX}$ upstream)	18%
Coolant density ratio, DR	1.20
$Re_{C,inlet}$	240,000

The density ratio (coolant density to mainstream density) of DR = 1.20 was maintained throughout the experiment. The corresponding coolant temperature to match this density ratio was around 250K, since the mainstream temperature was operating around 303K.

For the plots to be presented in this chapter, instead of showing the stream-wise location in terms of s/C, where s is the streamwise distance on the surface from the geometric leading edge and C is the blade chord length, we will be using x_1/d_1, the streamwise distance over diameter. $x_1 = 0$ is set to be the hole breakout location of row 1. The subscript number denote the relevance to row number. For example, M_1 and M_2 are blowing ratios of row 1 and row 2, respectively. In most following plots and figures, x and d terms are in terms of x_1 and d_1. The hole breakout location of row 2 is at $x_1 = 45d_1$. As noted earlier, d_1 is about 10% bigger than d_2, but we will be scaling parameters in terms of d_1 even after the second row.

3.2 TEST RESULTS

3.2.1 Single Row Test Results

The film effectiveness performance for the upstream row alone (row 1) is presented in Figure 3.1 (a) in terms of $\bar{\eta}$ (laterally averaged effectiveness) for M_1 = 1.5 - 3.0. The horizontal axis, x/d, is the stream-wise distance normalized by hole diameter of row 1. Note that sharp changes in slope for this distribution at x_1/d_1 = 10 and 50 are due to transition between cooled and uncooled regions in the blade model. The internal geometry of the blade was comprised of foam walls and air pockets, so whenever the inner structure transitioned from foam to air and vice versa, there was a small step in seen temperature. As noted earlier, conduction corrections were made, but they were not precise enough to completely cancel out these effects at transitions.

Among all the plots shown in this figure, the primary focus is on M_1 = 3.0 (red) and M_1 = 1.5 (blue). M_1 = 3.0 yielded the poorest performance that would be attributed to coolant separation from excessive blowing ratio. Beyond x_1/d_1 = 50 the film effectiveness increases. This can be attributed to coolant from the core of the coolant jet that was separated from the wall returning to the wall due to turbulent diffusion. On the other hand, M_1 = 1.5 corresponds to the maximum film effectiveness for row 1. The lateral distribution of coolant from row 1 for both blowing ratios is evident from the contours of η shown in Figure 2. A strong lateral variation is evident as far downstream as x_1/d_1 = 35, but the coolant distribution is relatively uniform farther downstream. Also evident from Figure 3.2 is that while coolant jets for the M_1 = 3.0 case seems to have completely separated from the surface by the time it passes row 2 (x_1/d_1 = 45), coolant jets from M_1 = 1.5 still have some footprints on the surface downstream of row 2.

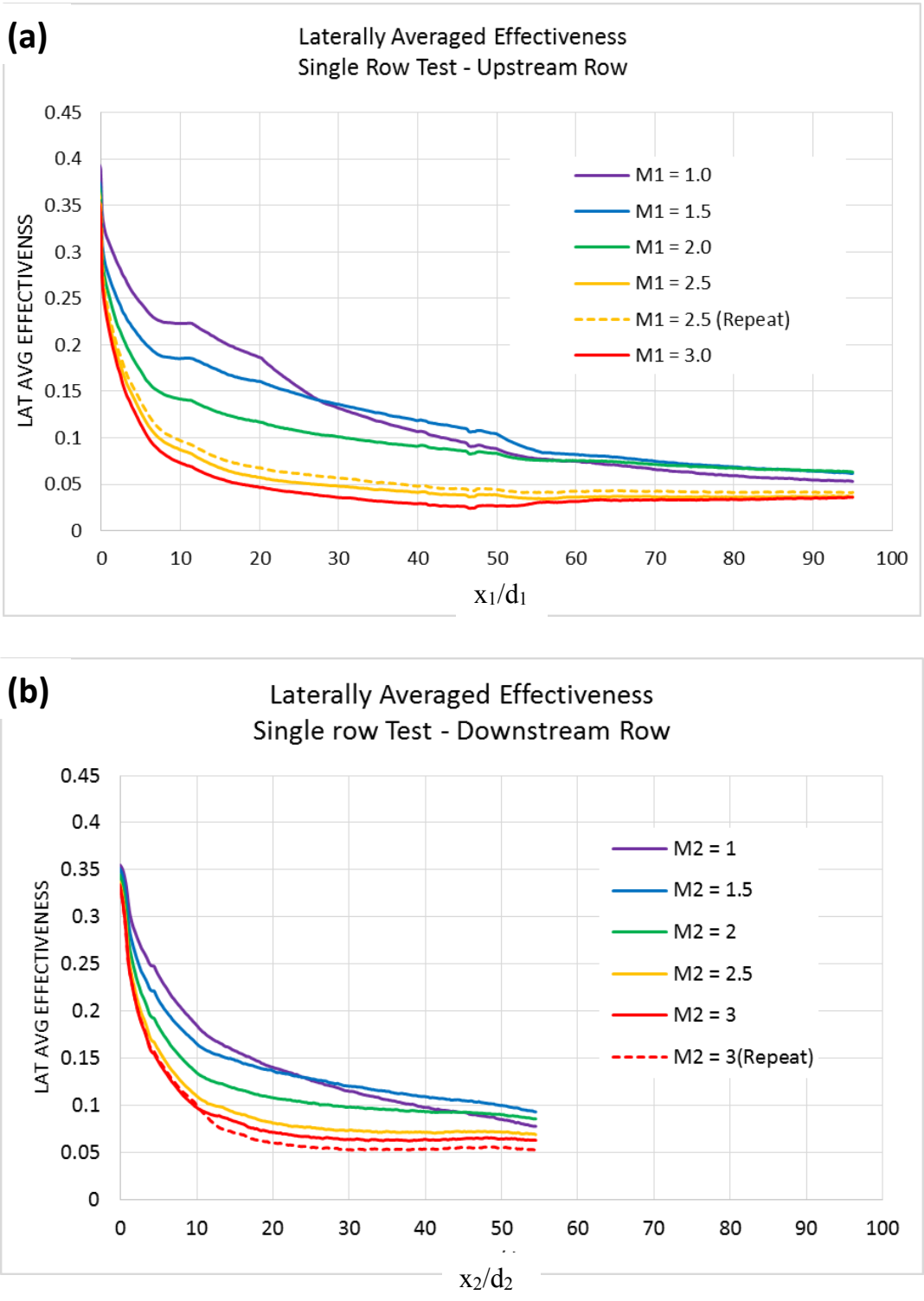

Figure 3.1: Laterally Averaged Effectiveness of Single Row Test - (a): Row 1 (b): Row 2

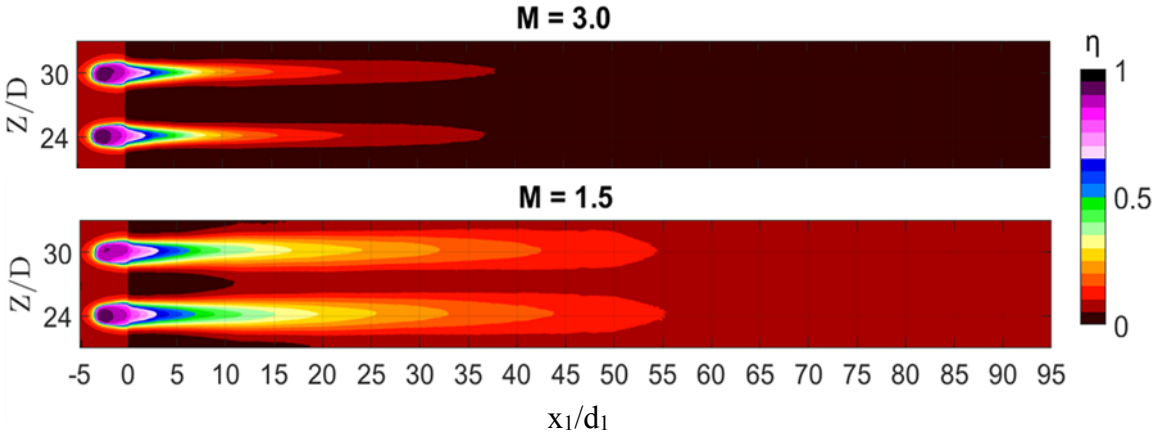

Figure 3.2: Effectiveness Contours at Row 1 for $M_1 = 3.0$ and $M_1 = 1.5$.

Next, the laterally averaged effectiveness $\bar{\eta}$ for the downstream row alone for $M_2 = 1.0$ to 3.0 are presented in Figure 3.1(b). As noted earlier, the hole breakout location for row 2 is located at $x_1/d_1 = 45$. Both $M_2 = 1.0$ and 1.5 yielded maximum film effectiveness, and a 50% decrease in film effectiveness was observed when blowing ratio was increased to $M_2 = 3.0$.The overall trend is the same from row 1, where $M_2 = 1$ performs best until approximately x/d = 20, and then $M_2 = 1.5$ outperforms downstream. For $M_2 = 2.0$, 2.5, and 3.0, the performance systematically decreases as blowing ratio is increased. But the gap between plots with different blowing ratios are smaller for row 2 then for row 1. While $M_1 = 1.0$ performs about 3 times better than $M_1 = 3.0$ at 10 hole diameters downstream in Figure 3.1(a), $M_2 = 1.0$ performs slightly less than 2 times better than $M_2 = 3.0$ in the same relative location in Figure 3.1 (b). Effectiveness contours are shown in Figure 3.3 for reference. Although M = 1.5 is still the best performing case and M = 3.0 is the worst performing case, the difference between M = 1.5 and M = 3.0 are not as drastic as what is

seen in Figure 3.2 for row 1. Test data from these single row effectiveness experiments for row 1 and row 2 were used for the superposition predictions.

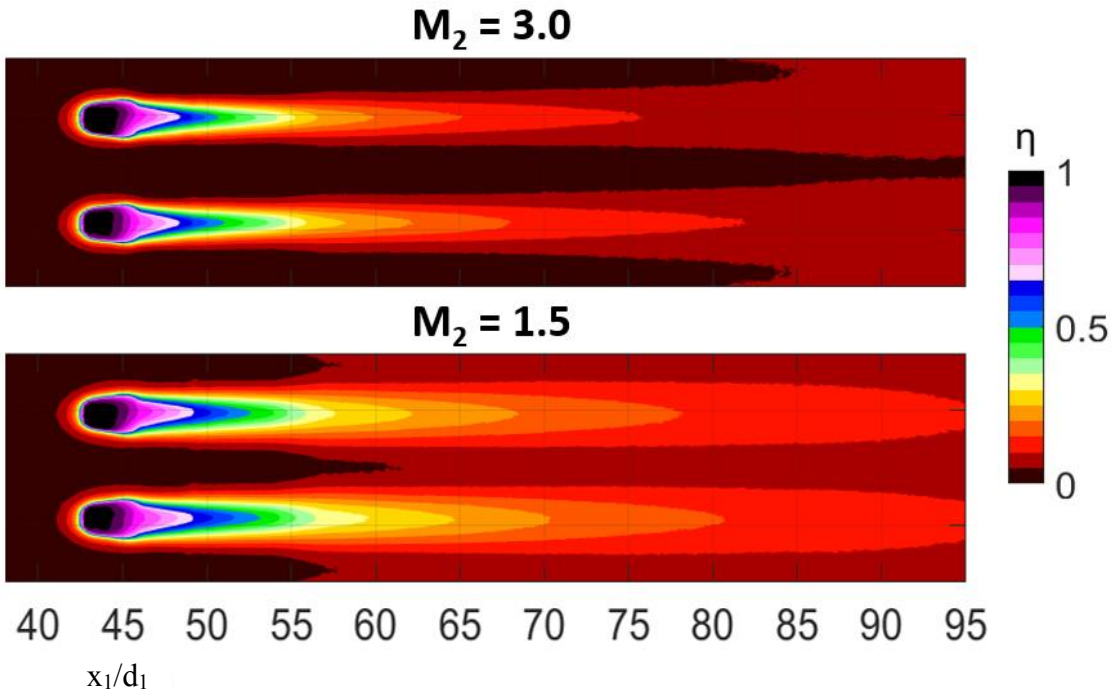

Figure 3.3: Effectiveness Contours of Row 2 for $M_2 = 3.0$ and $M_2 = 1.5$ (Note: x/d is in terms of x_1/d_1)

3.2.2 Results of Film Cooling Tests with Both Rows Operational

Two blowing ratios for row 1, $M_1 = 1.5$ and 3.0 were selected for the combined row tests. These two blowing ratios represented extreme cases in operating performance of the row 1. When $M_1 = 1.5$, the film cooling holes were at optimum performance with maximum film effectiveness far downstream. For $M_1 = 3.0$, the film effectiveness performance was very poor, which is attributed to significant jet separation from the surface. Although the film cooling tests were done with a range of $M_1 = 1.0 – 3.0$, these two extremes were selected for row 1 in a hope that it would provide insight on how well the Sellers model performs when upstream coolant jets are attached or detached from the surface. The latter case was of particular interest because of the potential of the downstream coolant jets interacting with the detached, overflowing coolant jets from upstream, resulting in better performance than the prediction by superposition model.

The film cooling performance with both rows operational with $M_1 = 3.0$ is shown in Figure 3.4. Figure 3.4 (a) shows the default case where the effectiveness was processed with downstream coolant temperature. Naturally, the film effectiveness in the region between row 1 and row 2 is due to film cooling from row 1 only. Therefore, the film effectiveness plots should all collapse if M_1 is fixed. Figure 3.4 (a) shows that all plots except one (blue line) collapses well in this region.

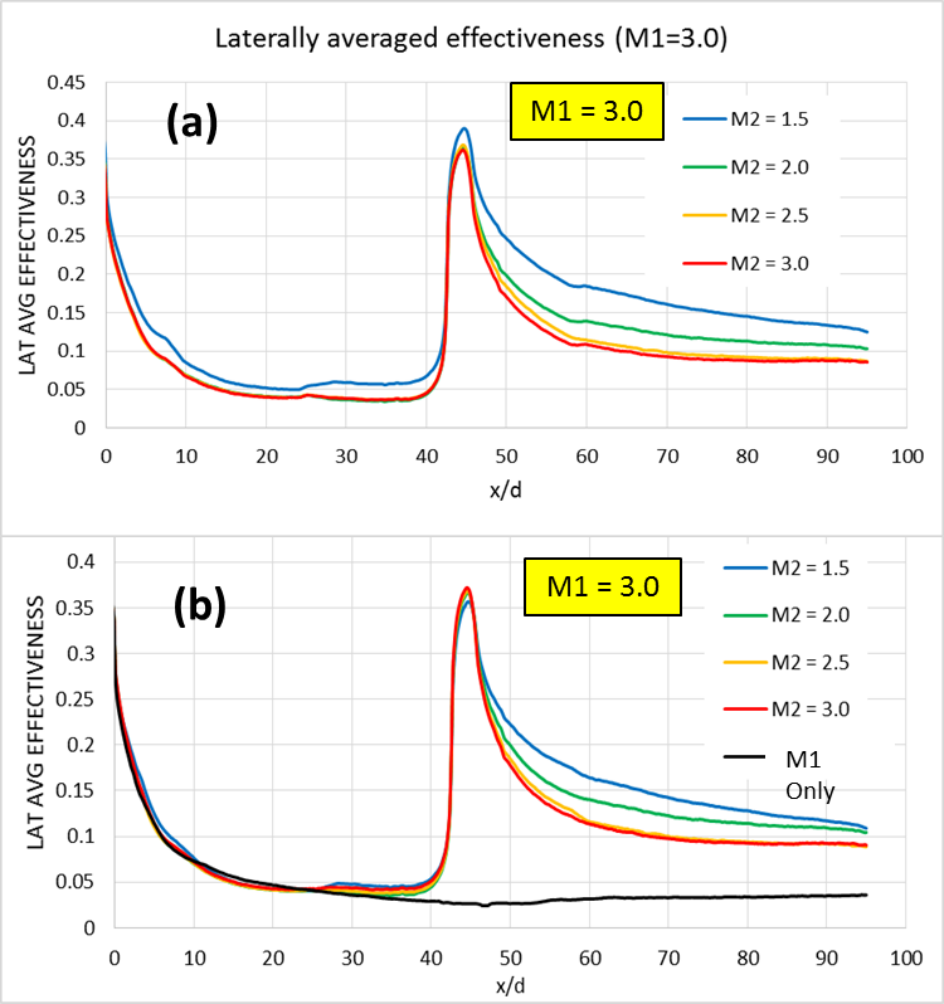

Figure 3.4: Laterally Averaged Effectiveness Plot with Both Rows Operational, $M_1 = 3.0$ (Top plot (a) is processed with row 2 coolant temperature, bottom plot (b) is processed with row 1 coolant temperature)

This outlier plot occurred because of temperature differences between upstream and downstream plenum. For this particular set with $M_1 = 3.0$ and $M_2 = 1.5$, the row 1 coolant temperature was about 3~4K lower than that of row 2. This was due to structure of the coolant control system, where individual flowrates were varied independently without control over individual temperature. When the coolant flow rate was low, the heat capacity

($\dot{m}c_p$) was lower, and the heat influx from surrounding environment had greater impact on the coolant temperature. Most of the times this issue was resolved by inducing heat influx to the colder pipe by using a heat gun on the valve, but this method was not enough to overcome the temperature difference for the particular set of $M_1 = 3.0$ and $M_2 = 1.5$ Since all effectiveness values were calculated based on the coolant temperature of row 2, the lower coolant temperature from row 1 showed higher effectiveness than usual. When processed with row 1 coolant temperature for adiabatic effectiveness η, all test points produced the same film effectiveness (Figure 3.4 (b)), and all of these matched closely with the results obtained from the single row test (black line).

Figure 3.5 shows the laterally averaged effectiveness with upstream blowing ratio of $M_1 = 1.5$. The film effectiveness downstream of row 2 showed a similar variation with increasing blow ratio as occurred with just row 2 operational, but naturally with increased film effectiveness levels due to added cooling effect from row 1 jets. Like the $M_1 = 3.0$ case, small variations of the effectiveness downstream of row 1 were observed. Processing with upstream plenum temperature, however, did not collapse the plots for this case. While this variation in effectiveness was not fully understood, day-to-day repeat experiments, as well as in-test experiments (Figure 3.6) show that this trend was consistent. It was concluded that this small variation would not affect the performance downstream of the second row, since the plots all collapse by $x_1/d_1 = 30$.

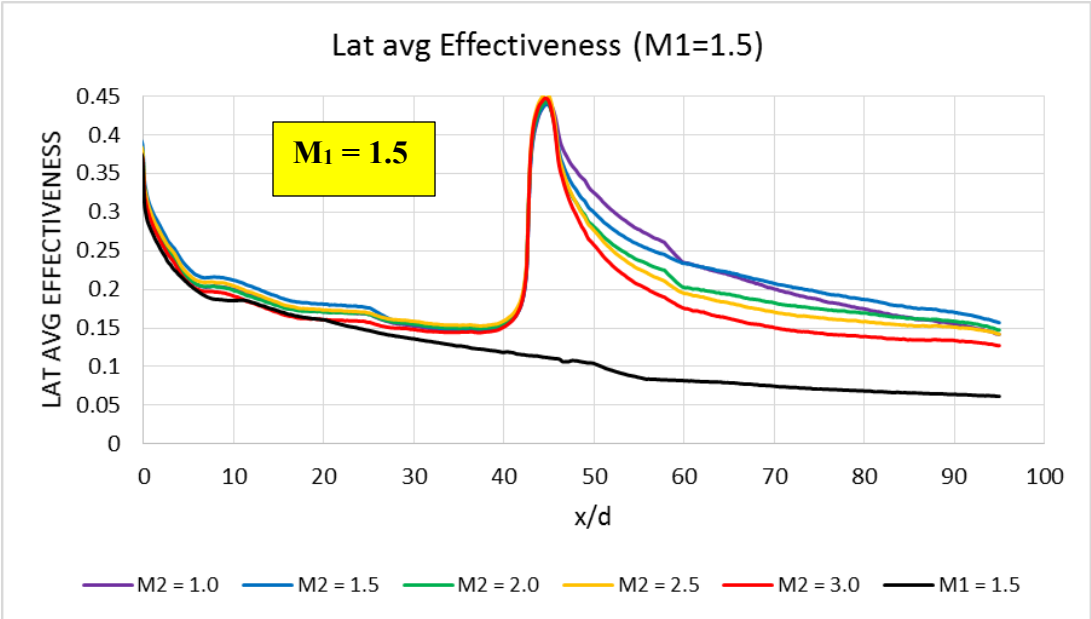

Figure 3.5: Laterally Averaged Effectiveness Plot, Both Rows Operational (M_1 = 1.5)

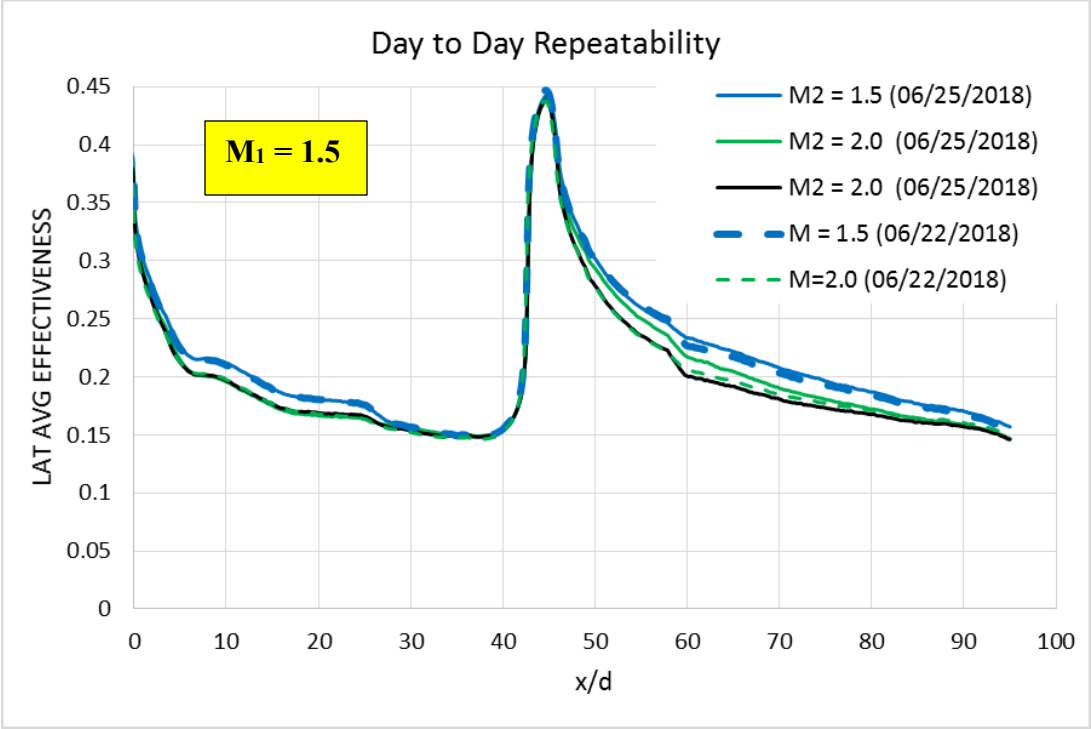

Figure 3.6: Plots Confirming Day-to-Day Repeatability and In-Test Repeatability

The primary purpose of this study was to determine whether the increases in film effectiveness downstream of row 2 were consistent with expectation using the Sellers superposition model. The contours of η shown in Figure 3.7 for the test cases of M_1 = 1.5 and 3.0 and M_2 = 1.5 shows how the coolant from the upstream coolant holes interact with the downstream holes. Because the centerlines of the upstream holes are in close alignment with the centerlines of the downstream holes, the coolant flow from upstream directly impacts the coolant jets from row 2.

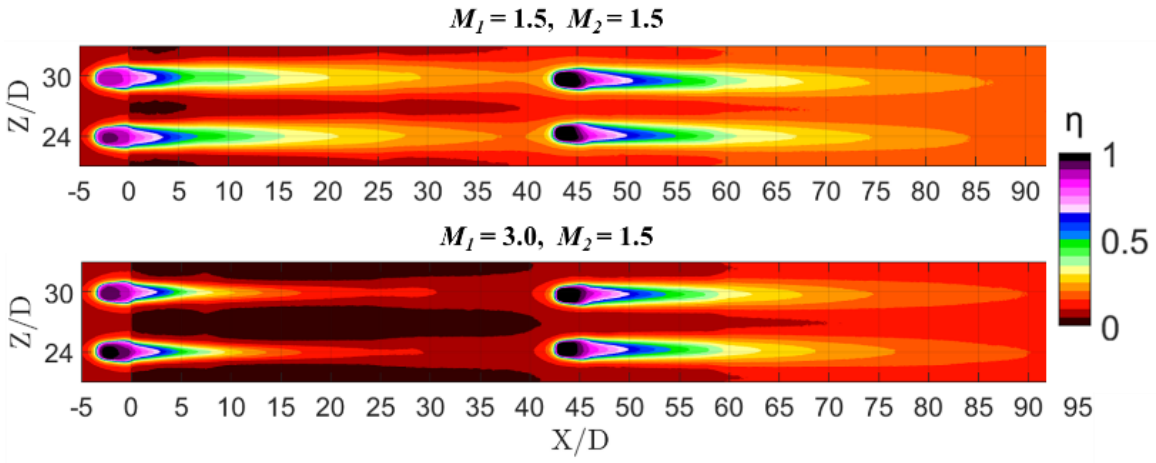

Figure 3.7: Effectiveness Contours for M_1 = 1.5 & 3.0, M_2 = 1.5

3.2.3 Evaluation of Sellers Superposition Predictions

Predictions of film effectiveness were made using the Sellers model for all test conditions. For clarity in the plots of these results, comparisons of predictions with measured distributions are presented for representative cases. For the case of the optimum blowing ratio from row 1, M_1 = 1.5, Figure 3.8 shows results for M_2 = 1.5 and 3.0. Besides

the comparison between prediction and measurements for film cooling from both rows of holes, for reference each figure shows the $\bar{\eta}$ distributions for single row operation with rows 1 and 2. For the M_2 = 1.5 case, Figure 3.8 (a) shows that the combined rows had about 70% higher film effectiveness than row 2 alone. The superposition prediction was slightly lower than the actual performance. For the M_2 = 3.0 case, Figure 3.8 (b) shows that the combined rows had about 100% increase in film effectiveness. Although the superposition model also predicted a substantial increase in film effectiveness, the predicted values were noticeably lower than actual values.

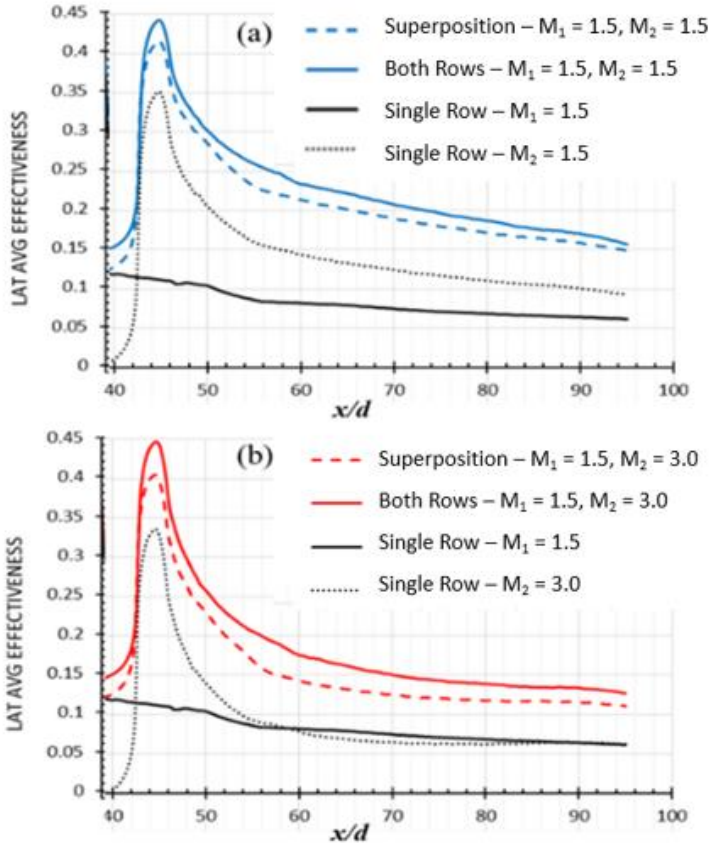

Figure 3.8: Comparison of Individual Row Performance, Superposition Prediction, and Actual Combined Effectiveness with M_1 = 1.5. (Top(a): M_2 = 1.5, Bottom(b): M_2=3.0)

For the case of the high blowing ratio from row 1, M_1 = 3.0, Figure 3.9 shows results for M_2 = 1.5 and 3.0. With M_1 = 3.0, beyond x_1/d_1 = 45 the film effective from the row 1 alone is quite low ($\bar{\eta}$ < 0.05). As shown in Figure 3.9, the combined rows had about 30% higher film effectiveness than row 2 alone. The superposition prediction closely matched the actual increase in film effectiveness for all blowing ratios of row 2.

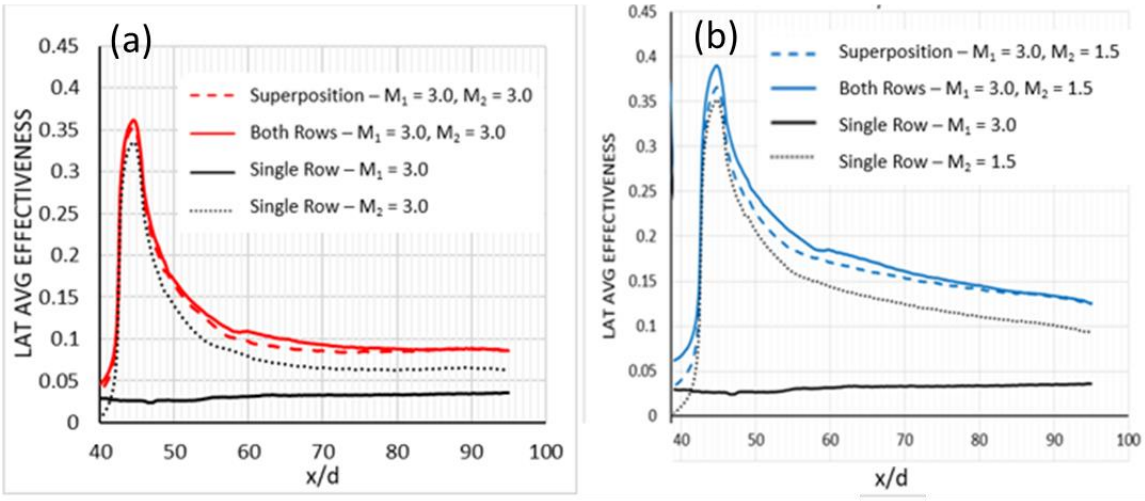

Figure 3.9: Comparison of Individual Row Performance, Superposition Prediction, and Actual Combined Effectiveness with M_1 = 3.0.
(Left(a): M_2 = 3.0, Right (b): M_2=1.5)

To provide more insight on the superposition predictions, comparisons are made between the measured and predicted lateral distribution of film effectiveness at a position 5d downstream of row 2 (x_1/d_1 = 50). This allows to determine the accuracy of the superposition predictions for peak effectiveness values and for low effectiveness values between coolant jets. The lateral distributions of η, measured and predicted, for blowing ratios of M_1 = 1.5 and M_2 = 1.5 & 3.0 are shown in Figure 3.10 (a) and (b), respectively.

Also presented in these figures for reference are the measured η distributions for single row operation with rows 1 and 2 that are used for calculating superposition predictions.

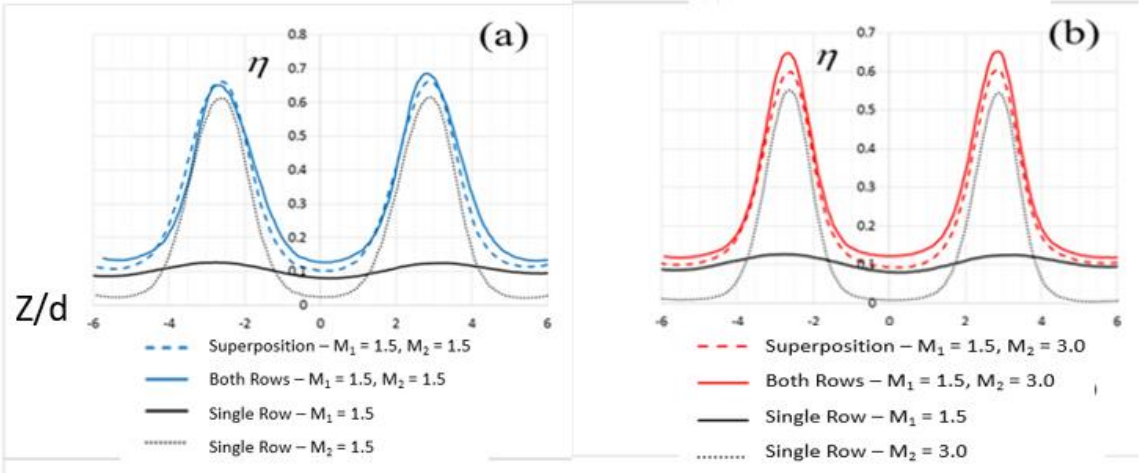

Figure 3.10: Lateral Distribution of Effectiveness at $x_1/d_1 = 50$ with $M_1 = 1.5$
(Left(a): $M_2 = 1.5$, Right(b): $M_2 = 3.0$)

For the $M_1 = 1.5$, $M_2 = 1.5$ case, the superposition prediction closely matched the peak values, but were noticeably lower in the low effectiveness region between coolant jets. Note that in the region between jets, the η values for row 1 alone was very low, around $\eta = 0.02$, so the superposition model would predict film effectiveness for the combined rows of holes just slightly higher than the η values for row 2 alone. However, the actual η values in this region is noticeably higher.

For the $M_1 = 1.5$, $M_2 = 3.0$ case shown in Figure 3.10 (b), the superposition predictions are noticeably lower at the peak positions and in the gap between peaks. The increased film effectiveness levels in these regions compared to the superposition predictions might be attributed to higher levels of turbulence near the wall due to the upstream injection of coolant at row 1. This higher level of near wall turbulence might

increase effectiveness levels in the gaps between coolant jets due to increased lateral spreading. The increase in effectiveness in the peak regions for the $M_2 = 3.0$ case might be due to increased turbulence causing coolant from the separated coolant jet to move towards the wall.

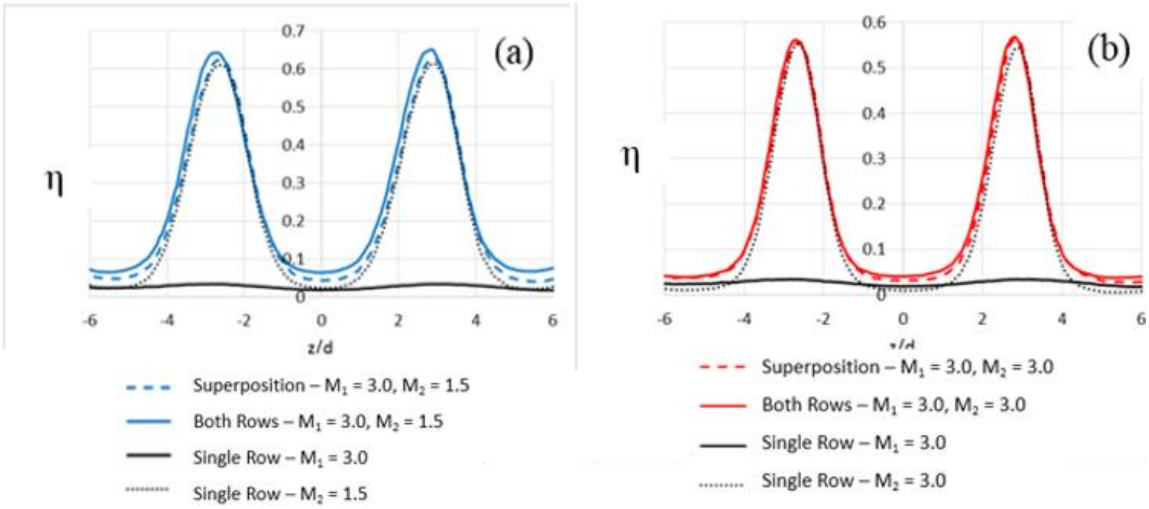

Figure 3.11: Lateral Distribution of Effectiveness at $x_1/d = 50$ with $M_1 = 3.0$
(Left(a): $M_2 = 1.5$ Right(b): $M_2 = 3.0$)

Lateral distributions of η, measured and predicted, for blowing ratios of $M_1 = 3.0$ and $M_2 = 1.5$ and 3.0 are shown in Figure 3.11 (a) and (b), respectively. For $M_2 = 1.5$, the superposition prediction was very close to the measured distribution, with a slightly lower predicted η value in the gap between jets. For $M_2 = 3.0$, the superposition prediction almost precisely matched the measured distribution. Although the good correspondence between the measurements and predictions for the $M_1 = 3.0$ case might be attributed to the very low values of η, it should be remembered that the coolant jet separated for this case. Consequently the core of the coolant jet is likely a short distance above the surface, and

had the potential of interacting with the coolant jets from row 2 and increasing η values compared to that predicted by superposition. This experiment showed that this does not happen.

In all lateral plots shown in Figure 3.10 and Figure 3.11, underprediction of valleys seem to be a consistent trend. The peaks tend to match well between superposition and measurement, except for Figure 3.10 (b), with low upstream blowing ratio and high downstream blowing ratio. In general, jet-to-jet interaction that was apparent at $M_1 = 1.5$ enhanced the downstream film effectiveness of row 2 more than what the superposition has predicted. In the case of $M_1 = 1.5$ and $M_2 = 3.0$, where high blowing ratio of M_2 normally has poor performance if operated alone, the combined downstream effectiveness benefitted effectiveness both in the jets and in between the jets.

The contours of measurement and superposition prediction with $M_1 = 1.5$ are shown in Figure 3.12. The contours are consistent with the trend we found from Figure 3.10 and 3.11. Combined effectiveness was higher than predicted effectiveness for $M_1 = 1.5$, especially in between the jets. For the case with $M_1 = 1.5$ and $M_2 = 3.0$, we see colder temperature (higher effectiveness) for both inside the jets as well as in between the jets.

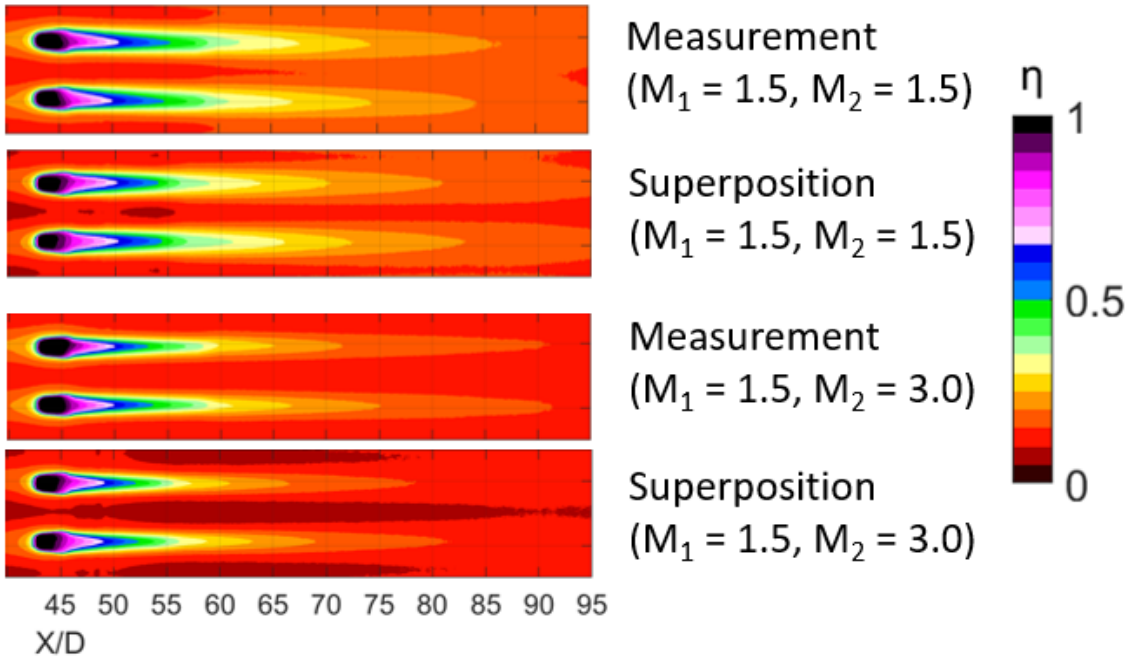

Figure 3.12: Effectiveness Contours for Comparing Measurement and Superposition (M_1 = 1.5, M_2 = 1.5, 3.0)

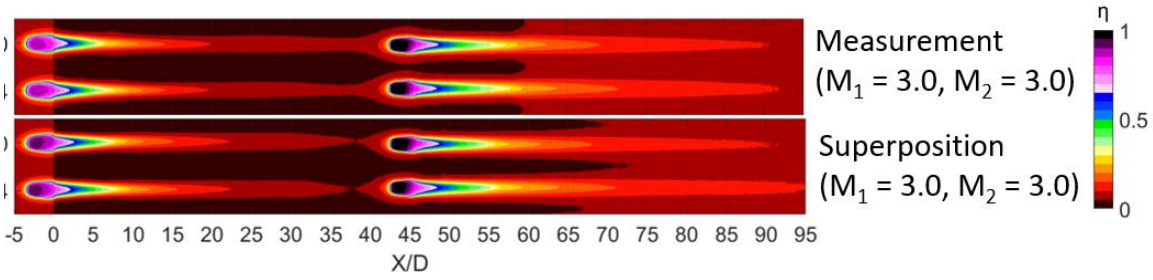

Figure 3.13: Effectiveness Contours of Measurement and Superposition for M_1 = 3.0 and M_2 = 3.0 case

On the other hand, contours shown in Figure 3.13 for M_1 = 3.0 case are similar. Combined effectiveness seems to have higher effectiveness in between the jets of row 2,

but overall, the width and length of the jets' footprints are consistent between superposition and actual measurement. The overflowing, detached jets from row 1 did not have much impact on the film cooling performance of row 2. Perhaps the jets from row 1 were too far from the surface, but this hypothesis cannot be confirmed unless a thermal field analysis is done on this model.

Chapter 4: Summary and Conclusions

4.1 Summary of Experimental Setup and Objective of this Study

This study was done using low speed, closed loop, infinite cascade facility of Turbulence and Turbine Cooling Research Laboratory (TTCRL) at the University of Texas at Austin. The test conditions were similar to the previous tests done in the same facility by Moore (2018) [15] with the existing large-scale blade model. The blade model was scaled from the model of computational study done by Kopriva et al [18]. The main difference was the placement of turbulence grid upstream, creating Tu = 18% at 0.2 C_{AX} upstream of the blade leading edge. The placement of turbulence grid changed the approach flow angle from 33.7° to 26.5°, so the side walls of the test section were adjusted to match the C_p distribution from low turbulence case. A 3mm diameter trip was placed upstream of the first row of holes to match the boundary layer thickness of δ_{99}/d_1 of 1.1, which is a condition commonly tested in TTCRL's flat plate facility.

The objective of this study was to evaluate the Sellers superposition method with actual measurements on the suction side of the blade model. There have been many studies done previously that investigated the accuracy of Sellers superposition model. However, most of the studies were done on a flat plate. The studies showed that Sellers method worked better for shaped holes than cylindrical holes, and for holes spaced far apart than closely spaced holes. Studies done on a blade model mostly used on arrays of closely spaced cylindrical holes, often investigating showerhead region or the effect of showerhead region to the pressure or suction side of the airfoil. To the best of the author's knowledge, there has been no experimental studies conducted that evaluates Sellers model on shaped holes spaced far apart (45d), on an airfoil model, investigating how row to row interactions affect combined effectiveness.

Since Sellers superposition model is a simplified thermal analysis, it was not likely to be accurate when jet to jet interactions were present. We hypothesized that in test cases in which coolant from the upstream of holes are separated before reaching downstream row of holes, the overflowing jets may interact with downstream coolant jets that could improve performance by bringing some of the coolant down to the surface. Another case of interest was when the upstream jets were still attached to the surface by the time they reached second row. It was not inherently obvious whether jet to jet interactions on the surface would improve or worsen the performance after the second row than what is predicted by Sellers model.

4.2 TEST PROCEDURE AND RESULTS

Single row tests with varying blowing ratios (M = 1.0 – 3.0) were first conducted, and these data were used to predict the combined effectiveness of both rows using Sellers superposition method. Then, the predictions were compared to actual measurements with both rows operational. Based on the single row test of the upstream row, two blowing ratios from upstream rows were selected, M_1 = 1.5 and M_1 = 3.0. M_1 = 1.5 was the optimum blowing ratio for row 1, and it represented a test case where the coolant jets from row 1 performed well beyond the location of row 2. It was likely that when both rows were operated at the same time, coolant from row 1 would be interacting with coolant ejecting from row 2. On the other hand, M_1 = 3.0 performed the poorest of all blowing ratios tested on row 1. The high blowing ratio likely caused an early separation of the coolant jet, resulting in negligible effectiveness downstream of row 2 location. Therefore, this

represented a case where the coolant from upstream row was completely detached by the time it was flowing over row 2.

When both rows were operational, $M_1 = 1.5$ case performed better than what the superposition had predicted. The higher performance may be attributed to additional turbulence generated by the upstream coolant injection, causing increased lateral spreading of the coolant and reduced separation of the coolant jet.

For the $M_1 = 3.0$ case, the superposition predictions closely matched the measured film effectiveness distributions. This result indicated that any interaction with overflowing detached coolant jets from the upstream row of holes had little effect on enhancing film effectiveness. It was also possible that the jets from row 1 were detached too far from the surface to be interacting with coolant jets of row 2.

Some insights were gained by looking at lateral distribution at certain location, $x_1/d_1 = 50$. In all cases, the superposition predictions underpredicted the valleys in effectiveness levels. For the $M_1 = 3.0$ case, this difference was negligible and did not show apparent underprediction in laterally averaged plots. For the $M_1 = 1.5$ case, this difference eventually led to underprediction of laterally averaged effectiveness, and underprediction of the peaks were also observed at high downstream blowing ratios.

4.3 FUTURE WORK

Several hypotheses were made in this study. It was likely that the upstream coolant jet was completely detached from the surface at high blowing ratio of $M_1 = 3.0$, but we did not have a good idea of how far the core of the jet would have been from the surface, and how much of it dissipated into the mainstream. It was found that for $M_1 = 1.5$ case, the

combined effectiveness performed better than what was predicted by Sellers superposition method, but how exactly the hydrodynamic effects caused better effectiveness between the jets is not fully understood. To have a more in-depth understanding about how jet to jet interaction affects the combined performance, the author recommends having thermal field measurements made on the suction side of the model.

Infrared cameras seeing different temperature in the overlap region was also a small issue in the study. In principle, calibration of IR cameras should have resulted in same temperature reading in the overlap region. Many hypotheses were made to explain the discrepancy, such as reflection effects of cold surface from upstream or downstream, deterioration of salt-crystal window, camera focus, and inaccurate temperature reading from large copper coupons in the calibration process. However, these hypotheses were neither confirmed nor disproved. We concluded that small upstream variation would not have affected downstream performance of the second row, which was the focus area of our study. Nevertheless, more investigation needs to be done to resolve and explain this issue.

REFERENCES

[1] D. G. Bogard and K. A. Thole, "Gas Turbine Film Cooling," *Journal of Propulsion and Power,* pp. 249-270, 2006.

[2] [Online]. Available: (https://www.ge.com/reports/post/115132114280/bringing-back-the-bling-new-process-recovers/).

[3] C. Saumweber and A. Schulz, "Effect of Geometry Variations on the Cooling Performance of Fan-Shaped Cooling Holes," *ASME Journal of Turbomachinery,* vol. 134, no. 6, 2012.

[4] J.-C. Han, "Recent Studies in Turbine Blade Cooling," *International Journal of Rotating Machinery,* vol. 10, no. 6, pp. 443-457, 2004.

[5] J. P. J. Sellers, "Gaseous Film Cooling with Multiple Injection Stations," in *AIAA*, 1963.

[6] A. K. Sinha, D. G. Bogard and M. E. Crawford, "Gas Turbine Film Cooling: Flowfield Due to a Second Row of Holes," in *J. Turbomach* , 1990.

[7] M. K. Harrington, M. A. McWaters, D. G. Bogard, C. A. Lemmon and K. A. Thole, "Full Coverage Film Cooling with Short Normal Injection Holes," *ASME Journal of Turbomachinery,* vol. 123, no. 4, pp. 798-805, 2001.

[8] L. Wang, X. Li, J. Ren and H. Jiang, "Effect of Row Spacing on the Accuracy of Film Cooling Superposition Method," in *GT 2018*, Oslo, Norway, 2018.

[9] C. Saumweber and A. Schulz, "Interaction of Film Cooling Rows: Effects of Hole Geometry and Row Spacing on the Cooling Performance Downstream of the Second Row of Holes," in *ASME Turbo Expo*, 2004.

[10] J. B. Anderson, J. R. Wrinka, D. G. Bogard and M. E. Crawford, "Evaluation of Superposition Predictions for Showerhead Film Cooling on a Vane," in *Proceedings of ASME Turbo Expo 2014*, Dusseldorf, Germany, 2014.

[11] M. D. Polanka, M. I. Ethridge, M. J. Cutbirth and D. G. Bogard, "Effects of Showerhead Injection on Film Cooling Effectiveness for a Downstream Row of Holes," in *Proceedings of ASME Turbo Expo 2000*, Munich, Germany, 2000.

[12] M. I. Ethridge, M. J. Cutbirth and D. G. Bogard, "Effects of Showerhead Cooling on Turbine Vane Suction Side Film Cooling Effectiveness," *ASME Heat Transfer Division (HTD),* vol. 366, pp. 69-78, 2000.

[13] S. Mhetras, J.-C. Han and R. Rudolph, "Film-Cooling Effectiveness from Shaped Film Cooling Holes for a Gas Turbine Blade," in *Proceedings of ASME Turbo Expo 2008*, Berlin, Germany, 2008.

[14] K. F. Chavez, "Variable Incidence Angle Film Cooling Experiments on a Scaled Up Turbine Airfoil Model," 2016.

[15] J. D. Moore, "Film Effectiveness Performance for a Shaped Hole on the Suction Side of a Scaled-Up Turbine Blade," 2018.

[16] G. R. Packard, "Experimentally Determined External Heat Transfer Coefficient of a Turbine Airfoil Design at Varying Incidence Angles," The University of Texas at Austin, Austin, 2015.

[17] P. E. Roach, "The generation of nearly isotropic turbulence by means of grids," *International Journal of Heat and Fluid Flow,* vol. 8, no. 2, pp. 82-92, June 1987.

[18] J. E. Kopriva, G. M. Laskowski and M. R. H. Sheikhi, "Computational Assessment of Inlet Turbulence on Boundary Layer Development and Momentum/Thermal Wakes for High Pressure Turbine Nozzle and Blade," in *IMECE*, 2014.

[19] R. P. Schroeder and K. A. Thole, "Adiabatic Effectiveness Measurements for a Baseline Shaped Film Cooling Hole," in *ASME Turbo Expo 2014*, 2014.

[20] J. W. McClintic, J. B. Anderson, D. G. Bogard, T. E. Dyson and Z. D. Webster, "Effect of Internal Crossflow Velocity on Film Cooling Effectiveness - Part 1: Axial Shaped Holes," *ASME Journal of Turbomachinery,* vol. 140, 2018.

[21] D. C. Montgomery and G. C. Runger, Applied Statistics and Probability for Engineers, 2003.

[22] D. A. Kistenmacher, "Experimental Investigation of Film Cooling and Thermal Barrier Coatings on a Gas Turbine Vane with Conjugate Heat Transfer Effects," UT Austin, 2013.

[23] M. Kinell, E. Utriainen, H. N. Najafabadi, M. Karlsson and B. Barabas, "Comparison of Gas Turbine Vane Pressure Side and Suction Side Film Cooling Performance and the Applicability of Superposition," in *ASME Turbo Expo*, 2012.

[24] B. Kirollos and T. Povey, "An Energy-Based Method for Predicting the Additive Effect of Multiple Film Cooling Holes," 2013.

[25] H. Zhu, T. Guo and D. Xu, "Investigation of Film Cooling and Superposition Method for double Row Dustpan-Shaped Holes," in *Heat Transfer Asian Res.*, 2008.